Tracing the Scale of Fluid Flow in Subduction Zone Forearcs: Implications from Fluid-Mobile elements

Kristijan Rajič, Hugues Raimbourg, Austin M Gion, Catherine Lerouge, Saskia Erdmann

Chemical Geology 659 (2024) 122141

Contents lists available at ScienceDirect

Chemical Geology

journal homepage: www.elsevier.com/locate/chemgeo

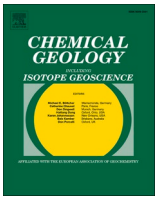

Tracing the Scale of Fluid Flow in Subduction Zone Forearcs: Implications from Fluid-Mobile elements

Kristijan Rajič [a,b,*], Hugues Raimbourg [a], Austin M. Gion [a,c], Catherine Lerouge [d], Saskia Erdmann [a]

[a] Institut des Sciences de la Terre d'Orléans, Université d'Orléans/CNRS/BRGM UMR7327, 1A Rue de la Ferollerie, Orléans 45100, France
[b] Department of Earth Sciences, Durham University, Science Laboratories, South Road, Durham DH1 3LE, UK
[c] Department of Earth Sciences, University of Oxford, 3 South Parks Road, Oxford OX1 3AN, UK
[d] B.R.G.M., BP 6009, Orléans 45060, cedex 2, France

ARTICLE INFO

Editor: Dr. Claudia Romano

Keywords:
Subduction zone
Fluid-mobile elements
Fluid-rock interaction
Fluid inclusions
LA-ICP-MS
Mass-balance calculations

ABSTRACT

Despite the importance of fluids in subduction zone processes, the extent of mass transfer and fluid circulation from the subducting plate through the forearc region remain unclear. To estimate the fluid budget and scale of fluid circulation in subducted sediments, we assess the distribution and retention of fluid-mobile elements (FME) in metamorphically equivalent metapelites from the Kodiak complex (Alaska) and the Shimanto Belt (Japan). The temperature range of interest is 230–350 °C, i.e., encompasses the base of the seismogenic zone. We examine the Li, B, Rb, Sr, Cs, and Ba concentrations in the bulk rock, as well as in fluid inclusions and individual minerals by (LA-) ICP-MS.

The whole-rock composition in metapelites from Kodiak shows no significant loss of FME, which is in contrast to Shimanto where between 10% and 55% of FME (particularly Li, B and Cs) are leached out of rocks. The FME budget in Kodiak is consistent with a redistribution of elements between metamorphic illite and chlorite, whereas in Shimanto the loss of Li, B and Cs as temperature increases is the result of decreasing concentrations in illite and chlorite. The semi-quantitative analysis of fluid inclusions is consistent with a significant enrichment in all analyzed trace elements relative to seawater and interstitial pore fluids of seafloor sediments.

Combining the fluid compositions with the whole-rock compositions, mass balance calculations were performed for B, Cs, and Ba. In the Kodiak complex the mass balance calculations are consistent with closed-system behavior, wherein the fluid is an insignificant reservoir for FME. Conversely, in the Shimanto Belt the mass balance calculations are consistent with open-system behavior, wherein large amounts of fluid percolated through rocks and the mass water-rock ratios correspond to 0.5–2.2. We infer that such an open system behavior was promoted by a larger amount of internal strain and the proximity to a large-scale fault zone. Moreover, fluid compositions observed in this study exhibit similarities to the composition of mud volcano fluids. This similarity is consistent with extensive, focused fluid circulation originating from depths of at least 15 km and ascending to the surface through a substantial damage zone associated with an out-of-sequence thrust.

1. Introduction

Fluids play a major role in many subduction zone processes, such as the element cycling between the different reservoirs of the Earth (Bebout, 1995, 2014, 2021; Hacker et al., 2003; Peters et al., 2017; Shervais and Jean, 2012; Tatsumi and Kogiso, 2003), seismicity (Audet and Schwartz, 2013; Behr and Bürgmann, 2021), or back-arc volcanism (Hacker, 2008; Schmidt and Poli, 2014; Stern, 2011). In addition to serpentinites and altered oceanic crust (Deschamps et al., 2013; John et al., 2011; Reynard, 2013; Rupke, 2004; Scambelluri et al., 2004a, 2019; Tenthorey and Hermann, 2004), sediments are an important carrier of volatiles, such as carbon dioxide or water (Bebout et al., 2013; Bekaert et al., 2020; Kerrick and Connolly, 2001; Rea and Ruff, 1996). Despite the critical role of fluids, the extent of fluid circulation in subducted material, as well as the quantity of fluids passing through permeable horizons, remain uncertain.

* Corresponding author at: Department of Earth Sciences, Durham University, Science Laboratories, South Road, Durham DH1 3LE, UK.
E-mail address: kristijan.rajic@durham.ac.uk (K. Rajič).

https://doi.org/10.1016/j.chemgeo.2024.122141
Received 30 November 2023; Received in revised form 30 April 2024; Accepted 3 May 2024
Available online 8 May 2024

Along with burial, load and temperature increase, sediments progressively lose the water they contain, following several processes (Saffer and Tobin, 2011). First, at shallow depths (typically <5 km), the volume of pore fluid is significantly reduced due to compaction and cementation (Kastner et al., 2014; Kominz and Pekar, 2001; Saffer and Tobin, 2011). Then, starting at ~50 °C with diagenetic reactions of hydrated silica phases and quartz and proceeding down to eclogite-facies conditions, successive metamorphic reactions result in a prograde decrease in mineral-bound water (Bebout, 2007; Hacker et al., 2003; Schmidt and Poli, 2014). The majority of fluids released early in the subduction history (<5 km) circulate along the subduction interface back to the ocean (You et al., 1995; Chan and Kastner, 2000; Saffer and Tobin, 2011), whereas in deeper regions (5–15 km) expelled fluids return to the ocean along out-of-sequence thrust faults in forearcs (Bangs et al., 1996; Bangs et al., 1999; Lauer and Saffer, 2012, 2015; Moore et al., 2001; Tobin et al., 2001; Ujiie, 2003; Vrolijk et al., 1991).

Dehydration fluids have compositions that differ significantly from seawater or original pore fluids, as a result of mineral reactions, such as the smectite-to-illite transformation (see the compilation by Kastner et al., 2014; Herviou et al., 2021). In particular, they are characterized by elevated fluid-mobile elements (FME) concentrations, even at low depths (Barnes et al., 2019b; Dia et al., 1999; Dimitrov, 2002; Martin et al., 1996; Westbrook and Smith, 1983). As a result, fluid-mobile elements have been extensively used to follow fluid and fluid-mediated transfers, including distinguishing between open or closed systems (Barnes et al., 2019b; Bebout et al., 2013; Bebout et al., 2007; Bebout et al., 1999), tracking dehydration reactions and loss of volatiles (Dragovic et al., 2012; John et al., 2011; Menzies et al., 2022; Peters et al., 2017; Scambelluri et al., 2004a), or tracing the scale of mass transfer and fluid circulation (Angiboust et al., 2014; Barnes et al., 2019a; Hoover et al., 2022; Ishikawa et al., 2008; Muñoz-Montecinos et al., 2021; Shervais and Jean, 2012; Zack and John, 2007).

Presumably, the FME budget is strictly controlled by the geothermal gradient, which governs the mineral reactions that occur along the prograde metamorphic path. For instance, Bebout et al. (2013) noted that in very cold subduction zones, like those preserved in the Western Alps (the gradient of ~8 °C/km), no major dehydration reactions have occurred down to ~80 km, thus preserving FME concentrations that are similar to those found in the potential sedimentary protolith. Conversely, metasedimentary rocks from the Catalina Schist, California, exhibit a progressive loss of FME (in particular B and Cs) along the prograde metamorphic path (Bebout et al., 2007). The B and Cs loss is attributed to the prograde devolatilization reactions, such as the progressive recrystallization of mica (Bebout et al., 2007). These studies belong to an abundant literature focused on tracking mass and fluid transfer in metamorphic series of rocks for temperature conditions above ~300 °C, whereas little is known for the lower conditions of the seismogenic depth interval (Oleskevich et al., 1999). The base of the seismogenic zone is of particular interest with respect to the issue of FME transfers and fluid circulations, as this range of depths satisfies both conditions of (1) rock brittle behavior, enabling a permeable crack network to form and (2) temperatures high enough for efficient fluid-rock interactions.

To elucidate FME and fluid mobility in the seismogenic domain of subduction zones, this work focuses on FME concentrations and budgets (Li, B, Rb, Sr, Cs, and Ba) in metasedimentary units from two paleo-accretionary complexes, the Kodiak complex and Shimanto Belt. This study builds upon earlier research concerning mineral reactions within the same complexes (Rajič et al., 2023b), which demonstrated the absence of dehydration reactions and the preservation of the major chemical composition in the range 230 to 350 °C. In the present work, we examine the evolution of FME budgets as a function of peak-metamorphic temperatures from 230 to 350 °C, by using a combination of three datasets: FME concentrations of whole-rock, individual metamorphic phases, and vein-hosted fluid inclusions. The Kodiak accretionary complex and the Shimanto Belt were selected for the following reasons: (1) Both localities are paleo-accretionary complexes, with the majority of the exposed rocks being basally underplated (Byrne and Fisher, 1987; Ditullio and Byrne, 1990; Fisher and Byrne, 1987; Sample and Moore, 1987; Taira et al., 1982; Ujiie, 1997). (2) Both contain rock units that have experienced a range of (near-) peak metamorphic conditions that correspond to the seismogenic zone and its down-dip limit (from ~230 °C up to ~350 °C; Vrolijk et al., 1988; Rowe et al., 2009; Raimbourg et al., 2014, 2021; Palazzin et al., 2016; Rajič et al., 2023a). At each locality, syn-subduction veins with primary fluid inclusions associated with a main deformation event have been observed (Raimbourg et al., 2021; Rajič et al., 2023b). (3) Units at each locality have lithological and mineralogical similarities, as well as similarities in deformation style (Raimbourg et al., 2014; Rajič et al., 2023a). (4) The primary distinction between these two complexes is that units from the Kodiak complex are situated at a considerable distance from any large-scale fault zones. Conversely, selected units in the Shimanto Belt are separated by the out-of-sequence thrust, the Nobeoka Tectonic Line (Kondo et al., 2005). The NTL was active significantly after the deposition ages of the unit in the hanging wall (Foliated Morotsuka; Fisher et al., 2019). As a result, this study provides (i) insights into fluid-rock interactions in subducted sediments at temperatures <350 °C and their impact on the chemical composition of pore fluids, as well as (ii) a framework for fluid circulation and mass transfer on the cm- to the multi-km scale.

2. Sampling areas

2.1. Kodiak accretionary complex

The Kodiak accretionary complex represents a well described paleo-accretionary complex that consists of coherent slices of metasedimentary units and tectonic mélanges (Fig. 1a), decreasing in age towards the modern trench (Byrne and Fisher, 1987; Connelly, 1978; Moore et al., 1983; Plafker et al., 1994). The Late Cretaceous Kodiak Formation consists of deep trench sediments, and is divided into three belts (Landward, Central and Seaward Belts) based on variations in bedding, cleavage orientation and peak-metamorphic temperatures (Rajič et al., 2023b; Sample and Fisher, 1986). The Kodiak Landward Belt (KLB) consists of intercalations of sandstone/siltstone and shale beds (Fig. 2a), with occasionally disrupted strata closer to the Uganik Thrust (Fisher and Byrne, 1987; Rowe et al., 2009). Veins from the Landward Belt are Mode 1 quartz veins with an orientation that is approximately perpendicular to the bedding (Fig. 2a). Temperatures derived from Raman Spectroscopy of carbonaceous material (RSCM) of the Landward Belt in Uyak Bay range from 240 to 260 °C (Rajič et al., 2023a). The Kodiak Central Belt (KCB) consists of sub-horizontal foliated shale and sandstone layers that are characterized by either (i) top-to-the-trench or (ii) conjugate extensive faults and recumbent folds (Rajič et al., 2023a; Sample and Fisher, 1986; Sample and Moore, 1987). Veins used for this study are Mode 1 quartz-(calcite) veins, often in en échelon arrays (Fig. 2c; Raimbourg et al., 2021; Rajič et al., 2023b) and are characterized by crack-seal microstructures (Fisher and Brantley, 2014; Raimbourg et al., 2021). The Central Belt, examined in Seal Bay, experienced temperatures of ~330 °C and pressures of 0.30 ± 0.04 GPa that are inferred from RSCM and multi-phase equilibrium models (Raimbourg et al., 2021; Rajič et al., 2023b). The geothermal gradient is estimated to be between 20 and 30 °C/km (Rajič et al., 2023b). The Kodiak Seaward Belt (KSB) is characterized by intercalated sandstone and shale layers. This belt experienced strong NW-SE horizontal coaxial shortening (Rajič et al., 2023a; Sample and Moore, 1987). RSCM temperatures of the Seaward Belt range from 300 to 350 °C (Rajič et al., 2023a). Samples from the Kodiak Central and Seaward Belts experienced similar peak-metamorphic temperatures and consequently are treated together as the higher-grade units in the Kodiak complex, while the Kodiak Landward Belt constitutes the lower-grade unit. All samples from the Kodiak Formation used during this study are sampled at least 2

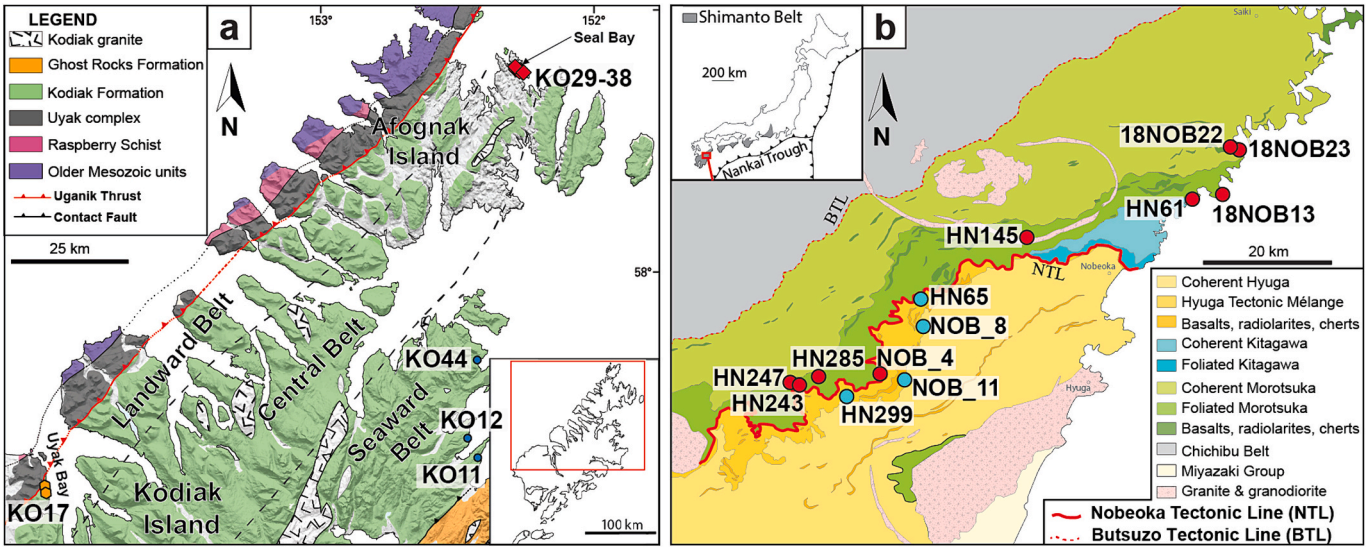

Fig. 1. Geological maps of (a) the Kodiak accretionary complex, Alaska, modified after Rajič et al. (2023a), and (b) the Shimanto Belt on Kyushu, Japan, modified after Raimbourg et al. (2021). The locations of individual samples used in this study are provided on each map.

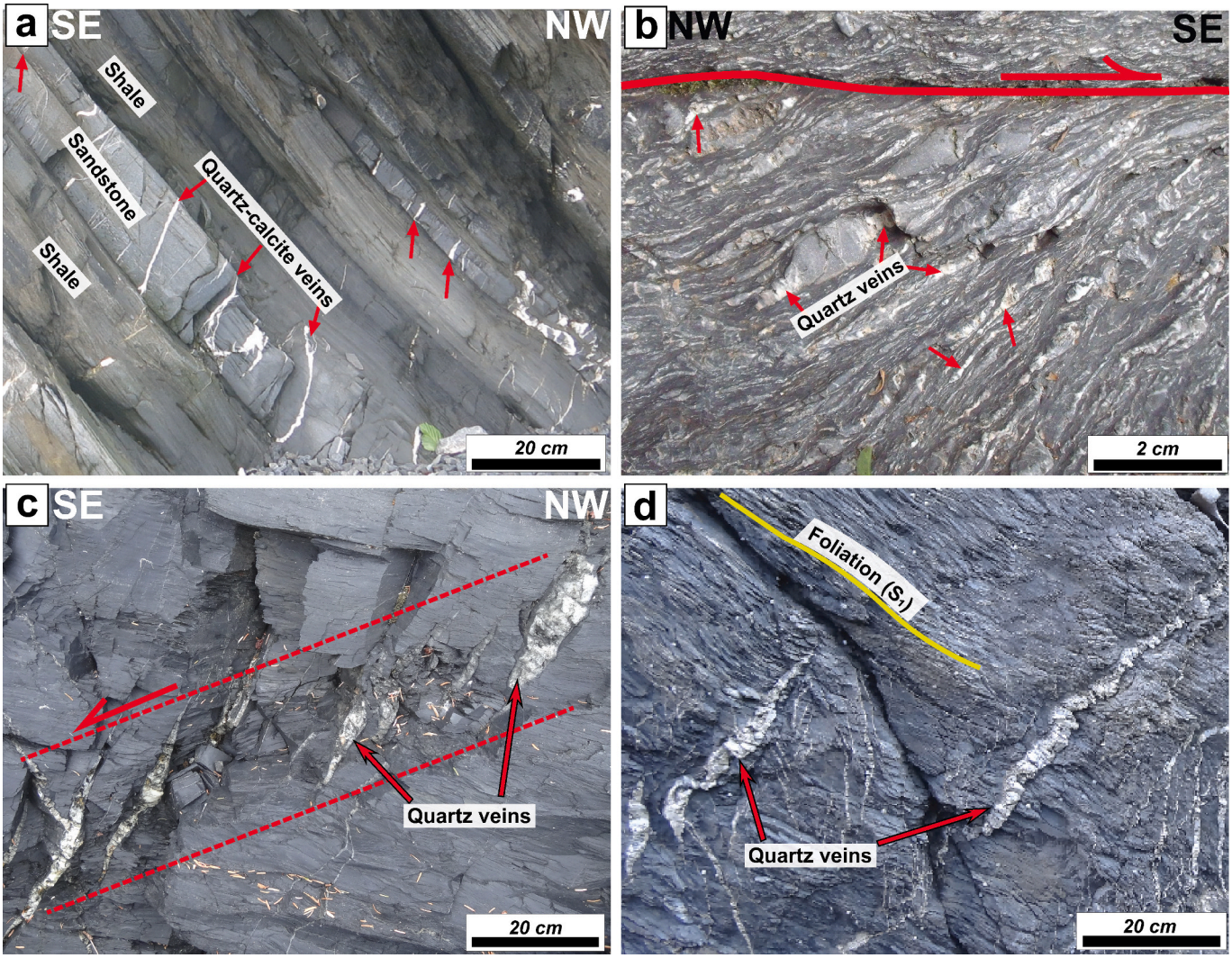

Fig. 2. Field photos of vein samples used in this study from the Kodiak complex (a and c) and the Shimanto Belt (b and d). (a) Mode 1 quartz-calcite veins in coherent portion of the Kodiak Landward Belt. (b) Quartz veins dominantly located in the sandstone lenses in strongly sheared sample from the Hyuga Tectonic Mélange. (c) A set of en échelon arrays from the Kodiak Central Belt. (d) An example of en échelon arrays from the Foliated Morotsuka.

km away from recognized large-scale fault zones (Fig. 1a).

2.2. Shimanto Belt, Japan

The Shimanto Belt is interpreted as a paleo-accretionary wedge (Taira, 1988) exposed on Honshu, Kyushu and Shikoku islands of Japan, with a general SW-NE trend of units parallel to the modern Nankai Through (Fig. 1b). The Foliated Morotsuka (FM) is the higher-grade unit of the Shimanto Belt. It comprises highly flattened sandstone and basaltic boudins embedded within a metapelitic matrix (Mackenzie, 1989; Raimbourg et al., 2014; Ujiie et al., 2018). Foliation is marked by the alignment of white mica and chlorite, which formed during vertical shortening (Kameda et al., 2011; Raimbourg et al., 2009). The Foliated Morotsuka records extensional tectonics at peak metamorphic conditions in the form of conjugate extensional shear bands (Raimbourg et al., 2014). Veins examined in this study are from en échelon arrays cutting across the foliations and are folded perpendicular to the foliation (Fig. 2d), which have been interpreted to have formed at peak metamorphic conditions (Raimbourg et al., 2021). Pressure-temperature conditions of the Foliated Morotsuka are estimated to be 0.3–0.5 GPa and 300–350 °C, respectively, and are based on RSCM and the metamorphic assemblages in basaltic lenses and multi-phase equilibrium model in metapelites (Palazzin et al., 2016; Rajič et al., 2023b; Toriumi and Teruya, 1988). Based on pressure-temperature results, the geothermal gradient is estimated to be around 20 °C/km (Rajič et al., 2023b; Toriumi and Teruya, 1988). The Foliated Morotsuka represents a hanging wall of the Nobeoka Tectonic Line (NTL), an out-of-sequence thrust (Kondo et al., 2005). The Hyuga Tectonic Mélange (HTM) is the footwall of the NTL and consists of strongly sheared sandstone lenses embedded in a pelitic matrix. The dominant syn-deformation veins are Mode 1 quartz veins perpendicular to the orientation of the sandstone lenses or mineralized shear bands (Fig. 2b). Based on RSCM, the peak temperature of deformation was 245 ± 30 °C (Palazzin et al., 2016), hence the Hyuga Tectonic Mélange is the lower-grade unit of the Shimanto Belt.

2.3. Mineralogy, textures and fluid inclusions of samples

Samples used for this study are extensively described in Rajič et al. (2023b). What follows is a summary of all relevant information. A sample list and peak-metamorphic temperatures-(pressures) are reported in Table A.1.

Whole-rock, major element compositions do not systematically change as temperature increases, consistent with the preservation of whole-rock composition and a potentially closed system. However, in restricted areas there is evidence of local mass transfer from the host rock to the veins. Main mineral phases in the host rocks in all samples are illite (21–48%), chlorite (0–24%), quartz (16–43%) and albite (5–26%). Minor smectite-illite mixed-layers are preserved only in lower-grade samples (1–5%). With increasing temperature, the major change in mineralogy is an increase in chlorite over other phyllosilicates (0–27% in low-grade samples vs 20–44% in higher-grade samples). In higher-grade samples, the smectite-to-illite transformation (later in the text referred as the illite recrystallization) is complete and is reflected by an increase in potassium in the interlayer site. Locally in higher-grade samples, quartz and albite are dissolved and reprecipitated in the veins. In lower-grade samples, from HTM and KLB, the grain size of illite and chlorite varies from 1 to 60 μm in length in the pelitic matrix and is up to 120 μm in length when in contact with quartz ribbons (Fig. 3a-b). At higher temperatures the grain size of chlorite and illite in the KCB range from 5 to 400 μm and 1 to 80 μm, respectively. The grain size of both phases is noticeably larger when in contact with the veins and is up to 775 μm (Fig. 3c). Similarly, samples from FM contain grains of illite and chlorite in the pelitic matrix that are characterized by significantly larger grain sizes of up to 1 mm (Fig. 3d).

Syn-subduction veins are characterized by different textures depending on the temperature at which they formed. Mode 1 quartz tension veins in lower-grade units are characterized by euhedral crystals with intercalation of high-luminescence (CL-blue) and low-luminescence (CL-brown) zones, which correlates to the aluminum concentration (Raimbourg et al., 2021). Veins in higher-grade units contain crack-seal textures with low-luminescent quartz. The quartz in all of the veins is characterized by dense populations of fluid inclusions (FIs), with local zones containing a low density of fluid inclusions (Fig. 4a-b). In lower-grade veins, two generations of primary FIs are observed: one-phase CH_4-rich and two-phase H_2O-rich FIs (Fig. 4c). Quartz in higher-grade veins contains only two-phase H_2O-rich FIs (Fig. 4d). The salinity of primary FIs also differs (Table A.1), wherein FIs in lower-grade quartz have salinities lower than that of seawater (~2 wt % NaCl eq.) and higher-grade FIs have salinities closer to or higher than that of seawater (~3.5 wt% NaCl eq.). The salinity of secondary FIs in all analyzed samples is <1 wt% NaCl eq.

3. Analytical and computational methods

3.1. Whole-rock trace element composition

Whole-rock trace element compositions were acquired for 16 samples from the Kodiak Formation (Landward, Central and Seaward Belt) and the Shimanto Belt (the Hyuga Tectonic Mélange and the Foliated Morotsuka). After removing any visible macro- and micro-veins, the metasedimentary samples were crushed in a mortar and washed with doubly distilled water. Subsequently, the sample powders were rinsed twice with doubly distilled water and then dried in an oven at 90 °C for 24 h. Final powder samples were analyzed at Actlabs (Activation laboratories Ltd. Ireland; analytical code ME-MS89L + B-MS89L). Samples (0.2 g) were fused with sodium peroxide at 670 °C and mixed with hydrochloric acid after cooling. Prepared solutions were analyzed by inductively coupled plasma-mass spectrometry. Boron has been analyzed separately by glassless digestion analysis to eliminate boron from labware. The detection limits of FME of interest are as follows: Li = 2 μg/g; B = 8 μg/g; Rb = 0.5 μg/g; Sr = 20 μg/g; Cs = 0.1 μg/g; and Ba = 2 μg/g. For remaining analyzed trace elements, the detection limits are given in Table A.2, as well as analyzed duplicates, standards (GIOP-111, AMIS0055, LR-LOI3, and LR-LOI5), and the sample blanks. The standards were measured as unknowns and were within 10% of accepted values (Table A.2).

3.2. Laser Ablation Inductively coupled Plasma Mass Spectrometry

3.2.1. Trace-element concentration in mineral phases

Laser Ablation Inductively Coupled Plasma Mass Spectrometry (LA-ICP-MS) was used to determine the trace element concentrations in major mineral phases (illite, chlorite, and albite in the pelitic matrix, and quartz and calcite in the veins). Sufficiently large grains (wider than 30 μm) for LA-ICP-MS analysis were carefully selected by using optical microscopy and SEM-BSE, as well as chemical mapping of thin sections (Rajič et al., 2023b). LA-ICP-MS analyses were conducted at CNRS Institut de Sciences de la Terre d'Orléans (ISTO) using a RESOlution-SE 193 nm ArF excimer laser with a S155 ablation cell coupled to an Agilent 8900 QQQ mass spectrometer. To determine trace element concentrations in illite, chlorite, albite, and vein calcite, the laser was operated at 3 Hz and a fluence of ~4 J/cm^2 on the sample surface, and a spot size of 10 μm in diameter. A SQUID was used to homogenize the ablation signal. For each phase and spot, the SiO_2 content measured by electron microprobe was used as an internal standard and NIST610 was used as an external standard. For calcite, predetermined CaO content measured by electron microprobe was used as an internal standard. NIST612 was also analyzed as unknowns for quality control. The analyzed isotopes were: ^{7}Li, ^{11}B, ^{51}V, ^{27}Al, ^{28}Si, ^{56}Fe, ^{60}Ni, ^{63}Cu, ^{66}Zn, ^{75}As, ^{85}Rb, ^{88}Sr, ^{93}Nb, ^{118}Sn, ^{133}Cs, and ^{137}Ba. Data reduction was performed with the software GLITTER™ (Van Achterbergh et al., 2001), wherein

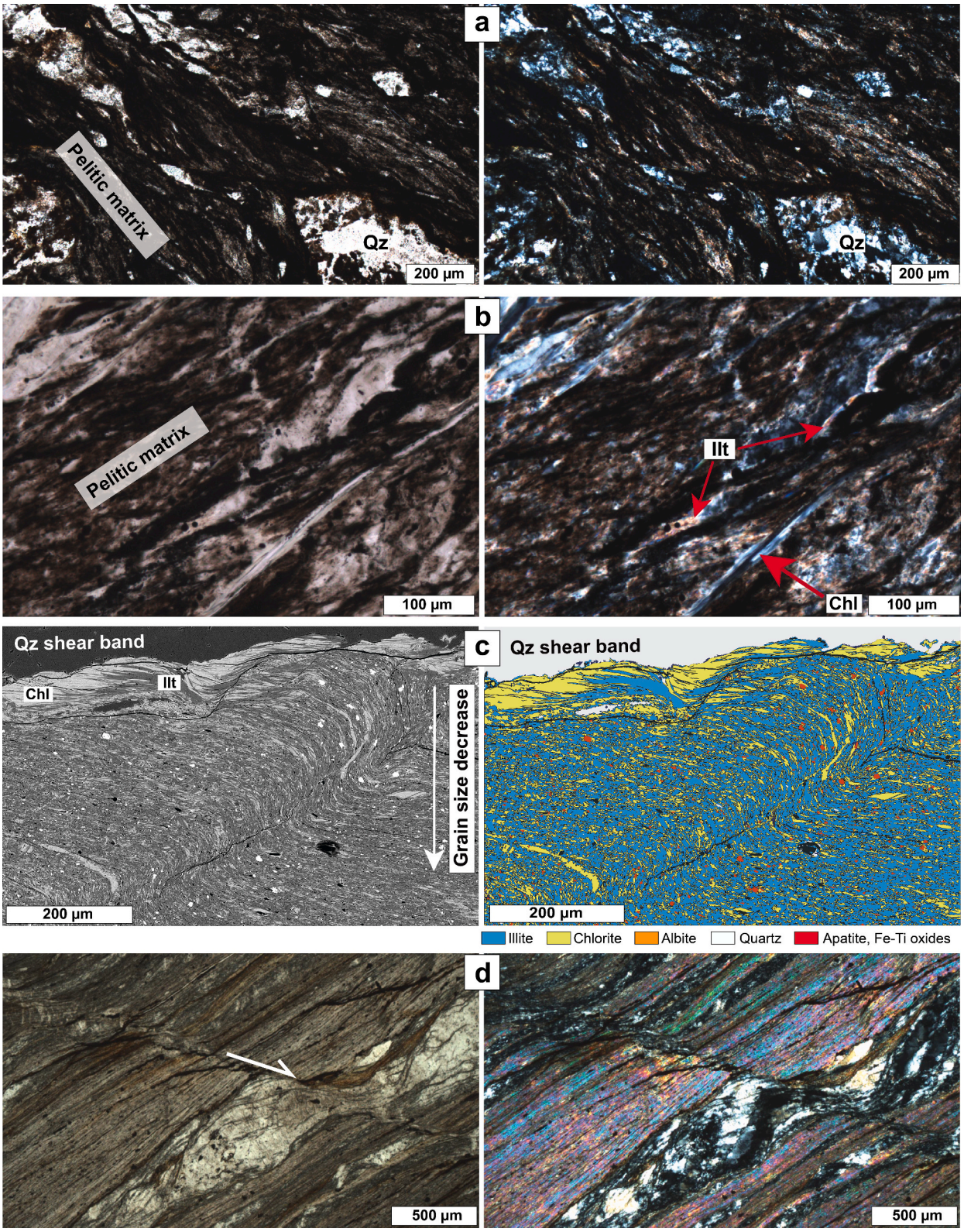

Fig. 3. Photomicrographs (optical microscope - a, b, d and SEM-BSE - c) images of metapelites from the Kodiak complex (a and c) and the Shimanto Belt (b and d). Low-grade metapelites characterized by intercalations of pelitic matrix and quartz ribbons from (a) the Kodiak Landward Belt (Sample KO17E) and (b) the Hyuga Tectonic Mélange (Sample HN299). Pelitic matrix contains fine-grained illite, chlorite, albite, and quartz, with only occasionally larger illite and chlorite grains. (c) A SEM-BSE (left) and a phase-map (right) of the matrix in the contact with a quartz shear vein, Kodiak Central Belt (Sample KO38). Note a grain size increase in the pelitic matrix towards the contact with the vein. (d) Metapelite with the pervasive foliation, the Foliated Morotsuka (Sample HN247). Note a significantly higher grain size than in previous samples.

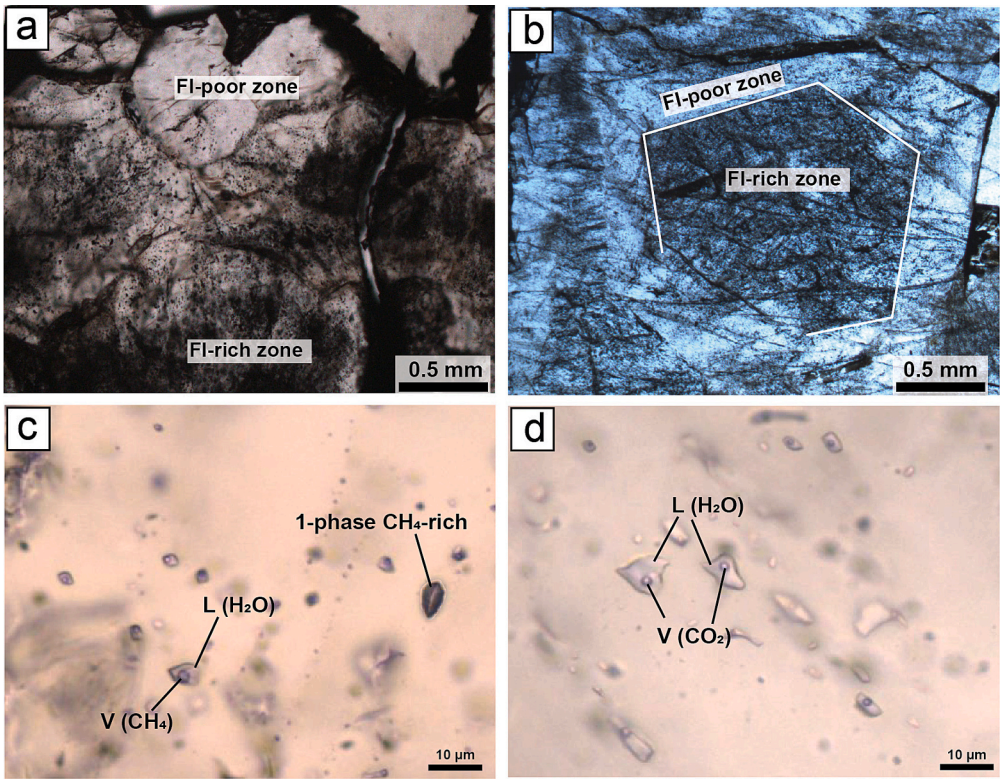

Fig. 4. Quartz and entrapped fluid inclusions from syn-subduction veins. (a-b) Quartz crystals characterized by FI-rich and FI-poor zones (Samples KO17 and KO33A2). Note that the FI-poor zone in (b) still contains fluid inclusions, but in comparison with adjacent FI-rich zone in significantly lower amount. (c) An example of coexisting one-phase CH_4-rich and two-phase H_2O-rich fluid inclusions in lower-grade veins (Sample KO17). (c) Primary two-phase H_2O-rich fluid inclusions with CO_2-(CH_4) vapor bubble in higher-grade veins (Sample KO33A2).

background and ablation signals were manually selected and a linear fit was applied to all standard data. The values of quality control (NIST612) are reported in the Table A.3.

3.2.2. *Bulk microanalysis of fluid inclusion populations*

The size of the FIs hosted in quartz in the studied samples rarely exceeds 10 μm and thus, the classical approach of analysis by laser ablation of individual FIs was not applicable. Instead, bulk microanalysis of FI populations, following the approach of Tuba et al. (2019), was utilized. Tuba et al. (2019) showed that this approach is in a good agreement with other methods for determining the chemical composition of FIs, such as microthermometric studies, decrepitation method or crush-leach techniques.

Doubly-polished thick sections of quartz were prepared with a thickness of ~200–250 μm. To avoid heating and volatilization of the glue during analysis, all superglue was removed after polishing by immersing samples in acetone for up to ~24 h and then rinsing repeatedly. The margins of the thick sections were subsequently fixed to a new glass plate with superglue. The laser was operated at a frequency of 5 or 10 Hz and a fluence of 8 J/cm^2 on the sample surface with a spot size of 50 μm in diameter. The isotopes that were analyzed were ^{7}Li, ^{9}Be, ^{11}B, ^{23}Na, ^{24}Mg, ^{27}Al, ^{28}Si, ^{39}K, ^{43}Ca, ^{47}Ti, ^{55}Mn, ^{56}Fe, ^{60}Ni, ^{63}Cu, ^{66}Zn, ^{75}As, ^{85}Rb, ^{88}Sr, ^{89}Y, ^{95}Mo, ^{118}Sn, ^{121}Sb, ^{133}Cs, ^{137}Ba, ^{182}W, ^{208}Pb, and ^{209}Bi. SiO_2 was used as the internal standard (100 wt%) and NIST610 was used as the external standard. NIST612 and BCR2G were also analyzed as unknowns for quality control.

In all veins that were examined, quartz displays distinct variations in FI abundance, which we refer to as FI-rich and FI-poor quartz zones (Fig. 4a-b). In FI-poor zones, quartz contains a significantly reduced quantity of FI (Fig. 4a-b). However, it is crucial to note that quartz is never entirely devoid of FIs (Fig. 4a-b). Before analysis, these FI-poor and FI-rich zones were qualitatively identified in each sample using optical microscopy.

The first step involves laser ablation analyses in FI-rich and FI-poor zones in quartz, to distinguish elements concentrated within the FIs from the elements hosted in the quartz crystal lattice. Given the higher FI density in the FI-rich zones, the elements contained within FIs will exhibit systematically higher concentrations compared to the FI-poor zones. The quartz zones selected for laser ablation were specifically targeted, such that the chosen areas predominately contained primary FIs and were without mineral inclusions. While secondary FIs are frequently present, their salinities are below 1 wt% NaCl eq. (Rajič et al., 2023b), indicating that the detected signal is primarily originating from primary FIs.

For elements displaying higher concentrations in FI-rich zones compared to FI-poor zones, it is assumed that these elements primarily reside within FIs rather than within the quartz crystal lattice. The composition of the primary FIs was determined by a standard charge-balance approach (Allan et al., 2005):

$$mNa + \sum_i n_i \times mX_i = mCl \quad (1)$$

where mX_i represents the concentration, in molality (mol/kg) and n_i represents the charge of each cation (X_i) other than Na, respectively. Eq. (1) can be transformed into:

$$mNa = mCl \times \left(1 + \sum_i n_i \frac{mX_i}{mNa}\right)^{-1} \quad (2)$$

where $\left(\frac{mX_i}{mNa}\right)$ stands for molal ratios of all elements of interest relative to sodium. Previously reported bulk salinities of the FIs (Raimbourg et al., 2018; Rajič et al., 2023b) were used to determine the total chlorine content of the inclusions (mCl). The molal ratios of all elements relative

to sodium $\left(\frac{mX_i}{mNa}\right)$ were determined by LA-ICP-MS for FI-rich zones. After determining both *mCl* and all molal ratios, the absolute concentration of sodium (mNa) and therefore the absolute concentration of all other elements mX_i were determined.

The main problem in the quantification procedure arises if major elements (as described in §4.3. – Na, K, or Ca) in the FIs are below the detection limit of the analyzed sample volume (which comprises both the signal from FIs and host quartz). Sodium and potassium are generally above detection limits, but calcium was at times below the detection limit. Therefore, the semi-quantitative results presented in this work are derived only for analyses where sodium, potassium and calcium concentrations were above detection limit.

3.3. Water-rock ratio calculations

To calculate mass water-rock (W/R) ratios present in the accretionary complexes, mass balance calculations were performed combining the FME whole-rock concentrations as well as recovered FME concentrations of fluid inclusions with theoretical porosity. The porosity of metapelitic rocks at the corresponding depths (>7 km) is expected to be below 5 vol% (Bray and Karig, 1985; Neuzil, 1994; Tsuji et al., 2006). Because the system is conservative and only mass exchange between the solid and fluid is considered, the change in the mass of an element in the solid and the fluid can be defined as

$$\left|\frac{m_i^{F,f} - m_i^{F,0}}{m_i^{S,f} - m_i^{S,0}}\right| = 1 \tag{3}$$

where $m_i^{F,f}$ is the mass of element i in the final fluid, $m_i^{F,0}$ is the mass of element i in the initial fluid, $m_i^{S,f}$ is the mass of element i in the final solid, and $m_i^{S,0}$ is the mass of element i in the initial solid, where final and initial state refer to higher and lower temperature conditions of the present study, respectively. For both the solid and the fluid, the mass of element i can be expressed as a concentration by

$$m_{Total}^j \cdot c_i^j = \mathrm{m}_i^j \tag{4}$$

where m_{Total}^j is the total mass of phase j (fluid or solid), c_i^j is the concentration of element i in phase j, and m_i^j is the mass of element i in phase j. Assuming that the total mass of the fluid and solid remains approximately constant at both final and initial stages, a valid approximation in conservative systems when considering trace elements, the concentrations of element i in the solid and the fluid can be expressed as

$$\left|\frac{\left(c_i^{F,f} - c_i^{F,0}\right)m_{Total}^F}{\left(c_i^{S,f} - c_i^{S,0}\right)m_{Total}^S}\right| = 1 \tag{5}$$

Finally, the concentrations of element i in the solid and the fluid are then related to the mass solid/fluid ratio with the following equation:

$$\left|\frac{\left(c_i^{F,f} - c_i^{F,0}\right)}{\left(c_i^{S,f} - c_i^{S,0}\right)}\right| = \frac{m_{Total}^S}{m_{Total}^F} \tag{6}$$

4. Results

4.1. Whole-rock trace element composition

Whole-rock trace element concentration data of FME of interest are presented in Table 1 and the concentrations are plotted as a function of peak-metamorphic temperatures in Fig. 5. The whole set of analyzed major and trace elements are reported in the Table A.2.

In the Kodiak complex, among all samples, lithium and boron concentrations range from 40 to 70 μg/g and from 60 to 130 μg/g, respectively (Fig. 5a-b). Concentrations of rubidium, strontium and barium range from 60 to 120 μg/g, 110 to 280 μg/g, and 560 to 1300 μg/g, respectively (Fig. 5c, d, e). Cesium concentrations are in the range of 3 to 7 μg/g (Fig. 5f; Table 1). In metapelites from the Shimanto Belt, lithium concentrations range from 50 to 70 μg/g in HTM and from 30 to 40 μg/g in FM (Fig. 5a; Table 1). Boron concentrations range from 160 to 200 μg/g in HTM and from 60 to 100 μg/g in FM (Fig. 5b). Concentrations of rubidium, strontium and barium are relatively consistent for the two units, ranging from 100 to 180 μg/g, 110 to 150 μg/g, and 430 to 700 μg/g, respectively, for all examined samples (Fig. 5c, d, e). Cesium concentrations are 9 to 11 μg/g in HTM and 5 to 6 μg/g in FM (Fig. 5f).

4.2. Distribution of FME among mineral phases

The average FME concentrations and standard deviation of mineral phases in each sample are reported in Table 2 and concentrations for

Table 1
Whole-rock trace element composition of studied metapelites from the Kodiak accretionary complex and the Shimanto Belt. Raman Spectroscopy of carbonaceous material (RSCM), K_2O and MgO results are from Rajič et al. (2023b).

	RSCM	K_2O	MgO	B	Li	Rb	Sr	Cs	Ba	B/K_2O	Li/K_2O	Rb/K_2O	Sr/K_2O	Cs/K_2O	Ba/K_2O	Li/MgO	B/Li	Rb/Cs
Sample	T (°C)	wt %	wt%	μg/g	μg/g	μg/g	μg/g	μg/g	μg/g									
Kodiak																		
KO17B	256	1.48	1.94	64	39	59.7	110	4.2	555	43.2	26.4	40.3	74.3	2.8	375.0	20.1	1.6	14.2
KO17C	256	2.84	2.26	118	40	120.5	110	7.1	1125	41.6	14.1	42.4	38.7	2.5	396.1	17.7	3.0	17.0
KO17D	258	2.37	2.08	78	57	96.3	280	3.8	1015	32.9	24.1	40.6	118.1	1.6	428.3	27.4	1.4	25.3
KO17E	240	2.62	2.18	139	55	105	190	5.8	978	53.1	21.0	40.1	72.5	2.2	373.3	25.2	2.5	18.1
KO33	333	1.94	2.83	115	52	93.1	130	4.2	1300	59.3	26.8	48.0	67.0	2.2	670.1	18.4	2.2	22.2
KO36	330	3.29	3.08	90	51	77.1	260	3.4	950	27.4	15.5	23.4	79.0	1.0	288.8	16.6	1.8	22.7
KO38	340	3.61	3.19	127	70	112.0	120	5.4	1195	35.2	19.4	31.0	33.2	1.5	331.0	21.9	1.8	20.7
KO11	300	2.82	3.29	122	54	83.4	200	3.7	923	43.3	19.2	29.6	70.9	1.3	327.3	16.4	2.3	22.5
KO12B	348	2.63	2.85	112	56	81.1	180	3.8	859	42.6	21.3	30.8	68.4	1.4	326.6	19.7	2.0	21.3
KO45C	345	2.63	2.85	78	51	68.5	230	3.5	818	29.7	19.4	26.1	87.5	1.3	311.0	17.9	1.5	19.6
Shimanto																		
HN64	238	3.29	1.98	195	68	164.5	110	10.5	704	59.3	20.7	50.0	33.4	3.2	214.0	34.3	2.9	15.7
HN85	242	1.44	1.49	155	53	179.0	120	9.0	664	107.6	36.8	124.3	83.3	6.3	461.1	35.6	2.9	19.9
HN299	228	2.80	1.80	167	54	167.5	150	10.1	655	59.6	19.3	59.8	53.6	3.6	233.9	30.0	3.1	16.6
18NOB23	341	3.04	2.44	97	44	106.0	110	4.9	430	31.9	14.5	34.9	36.2	1.6	141.5	18.0	2.2	21.6
HN285	321	3.08	2.07	63	26	182.0	130	6.2	664	20.5	8.4	59.1	42.2	2.0	215.6	12.6	2.4	29.4
HN243	335	3.00	1.74	65	28	144.5	110	5.4	531	21.7	9.3	48.2	36.7	1.8	177.0	16.1	2.3	26.8

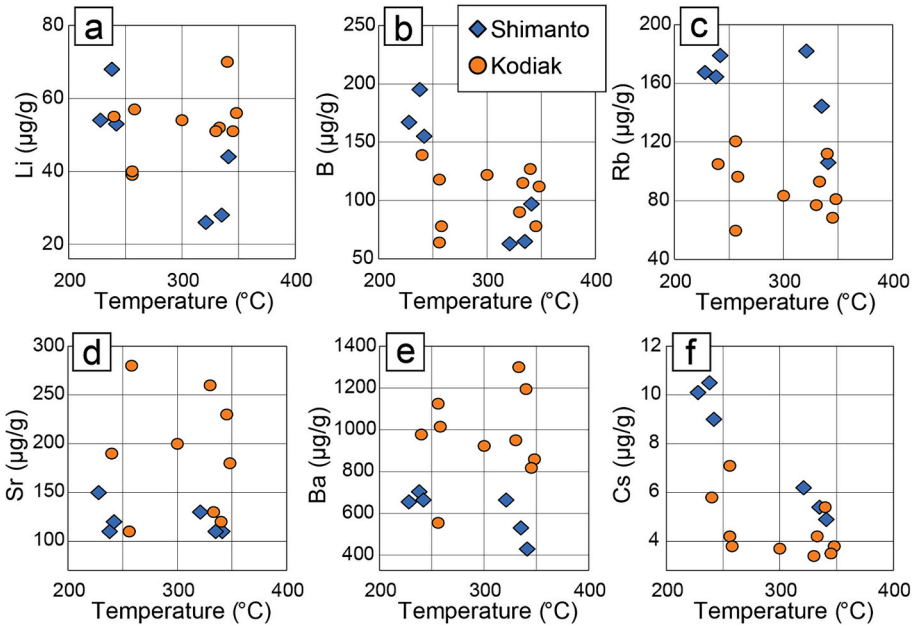

Fig. 5. Whole-rock FME concentrations in metapelites from the Shimanto Belt and the Kodiak accretionary complex as a function of peak-metamorphic temperatures: (a) Li; (b) B; (c) Rb; (d) Sr; (e) Ba; and (f) Cs.

illite and chlorite are also presented in Fig. 6. All analyses are presented in Table A.4.

Lithium. Lithium is mainly hosted in chlorite and illite (Fig. 6), and to a lesser extent in quartz from the veins (Raimbourg et al., 2021). In the KLB lithium concentrations in chlorite are 240 ± 20 µg/g and 50 ± 20 µg/g in illite. In the KCB, chlorite has a lithium concentration of 250 ± 90 µg/g (Fig. 6a) and illite has a lithium concentration of 30 ± 20 µg/g (Fig. 6b). In the Kodiak complex, chlorite shows retention or even slight lithium enrichment as temperature increases, whereas illite is characterized by comparable lithium concentrations (Fig. 6b). In the Shimanto Belt, lithium concentrations in chlorite are 320 ± 40 µg/g and 140 ± 20 µg/g for samples from HTM and FM, respectively, and in illite lithium concentrations are 90 ± 70 µg/g and 20 ± 20 µg/g for HTM and FM, respectively (Fig. 6b). In the Shimanto Belt, the lithium concentration decreases in both chlorite and illite as temperature increases (Fig. 6; Table 2). The vein quartz contains Li in concentrations from <30 µg/g in veins from KLB and < 6 µg/g in KCB, <110 µg/g in HTM down to <4 µg/g in FM (Raimbourg et al., 2021). Calcite from the veins contains <1 µg/g of lithium, with the majority of analyses being below detection limit (<0.1 µg/g; Table 2).

Boron. Boron is dominantly carried by illite and to a lesser extent by chlorite and albite. In the Kodiak complex, illite is characterized by boron concentrations of 140 ± 50 µg/g and 210 ± 40 µg/g for KLB and KCB, respectively. Chlorite from the Kodiak complex has boron concentrations of 10 ± 5 µg/g and 40 ± 30 µg/g for KLB and KCB, respectively (Fig. 6a). In the Shimanto Belt, boron concentrations in illite are 260 ± 60 µg/g and 150 ± 70 µg/g for samples from HTM and FM, respectively (Fig. 6b). Chlorite in units from the Shimanto Belt has low boron concentrations of 40 ± 30 µg/g and 5 ± 3 µg/g in HTM and FM, respectively (Fig. 6a). Albite from the KLB has boron concentrations of 20 ± 10 µg/g, whereas boron concentrations in albite from HTM are 50 ± 10 µg/g (Table 2). The behavior of boron is similar to that of lithium in illite and chlorite. In the Kodiak complex, boron is retained with similar concentrations between lower- and higher-grade illite and chlorite, whereas in the Shimanto Belt boron concentrations decrease in both illite and chlorite (Fig. 6a-b). Calcite in veins contains boron concentrations of up to 15 µg/g, yet the majority of analyses ranges from below detection limit (<1 µg/g) to 5 µg/g (Table 2).

LILE (Rb, Sr, Cs, and Ba). Major carrier minerals of large ion-lithophile elements are illite (Fig. 6b) and albite (Table 2). Rubidium concentrations in illite from the Kodiak complex are 190 ± 50 µg/g and 320 ± 30 µg/g in KLB and KCB, respectively (Fig. 6b). Illite from the Shimanto Belt shows slightly higher rubidium concentrations than in the Kodiak complex, with concentrations of 320 ± 50 µg/g and 400 ± 40 µg/g in illite from HTM and FM, respectively (Fig. 6b). Illite has strontium concentrations of 90 ± 40 µg/g in the KLB, 70 ± 40 µg/g in the KCB, 60 ± 40 µg/g in the HTM, and 30 ± 10 µg/g in the FM (Fig. 6b). Illite from KLB has barium concentrations of 1500 ± 400 µg/g and illite from the KCB has an average barium concentration of 2300 ± 300 µg/g (Fig. 6b). The average barium concentration in illite from HTM is 1100 ± 200 µg/g and illite from FM has a barium concentration of 1400 ± 100 µg/g (Fig. 6b). Cesium concentrations in illite are 8 ± 3 µg/g from KLB, 17 ± 3 µg/g from KCB, 18 ± 5 µg/g in samples from HTM, and 15 ± 3 µg/g from FM (Fig. 6b). Albite hosts LILE as well, but due to its small grain size only analyses on the lower-grade samples were performed. In samples from both KLB and HTM, albite contains low rubidium concentrations of 20 ± 20 µg/g and 40 ± 20 µg/g, respectively (Table 2). Measured concentrations of strontium are 240 ± 220 µg/g in KLB and 150 ± 80 µg/g in HTM, whereas barium concentrations are 200 ± 100 µg/g in KLB and 120 ± 90 µg/g in HTM (Table 2). The lowest concentrations among LILE are for cesium, which are <2 µg/g in KLB and 3 ± 2 µg/g in HTM.

Calcite from the veins contains no significant rubidium or cesium concentrations (<10% of the measurements have concentrations above the detection limit; concentrations <1 µg/g). Barium concentrations in calcite range from 1 to 45 µg/g (average 9 µg/g), whereas strontium concentrations are the highest in calcite among LILE, ranging from 0.16 to 1.06 wt% (Table 2).

4.3. Major and trace elements of fluid inclusion populations

A total of 393 LA-ICP-MS spot analyses were performed for FI-rich quartz domains and 208 for FI-poor quartz (Table A.5) in order to determine which elements are hosted within FIs and which ones are hosted in the quartz crystal lattice. Estimated concentrations of Be, Ni, Zn, As, Y, Mo, Sn, Sb, W, Pb, and Bi are below or very close to the detection limit without any systematic difference between FI-poor and FI-rich zones. FI-rich zones are characterized by systematically higher

Table 2
The average concentrations and standard deviation of trace elements in chlorite (chl), illite (ill), albite (ab), and calcite (cc) analyzed by LA-ICP-MS.

	#	Phase		Li	B	V	Ni	Cu	Zn	As	Rb	Sr	Nb	Sn	Cs	Ba
				μg/g	μg/g	μg/g	μg/g	μg/g	μg/g	μg/g	μg/g	μg/g	μg/g	μg/g	μg/g	μg/g
Kodiak Landward Belt																
KO17A	34	ill	Av.	70	150	290	60	30	100	30	190	100	8	4	9	1400
			SD	40	80	80	30	20	60	20	50	300	8	2	3	400
	15	ab	Av.	5	20	10	60	10	10	–	20	240	–	–	–	200
			SD	2	10	10	20	8	10	–	20	220	–	–	–	100
KO17E	26	ill	Av.	70	150	300	60	30	100	30	200	100	4	3	8	1600
			SD	40	30	60	50	20	90	20	30	90	4	1	2	300
	6	chl	Av.	190	20	150	140	25	300	7	20	20	1	2	2	60
			SD	50	10	50	40	8	100	4	10	9	1	1	1	20
KO17H	15	cc	*Av.*	0.15	1	–	–	0.4	1.8	0.19	0.04	6200	–	–	–	21
			SD	0.07	0.4	–	–	0.3	0.6	0.07	0.02	900	–	–	–	4
Kodiak Central Belt																
KO29A	24	ill	Av.	100	210	350	90	50	130	9	310	60	1	6	17	2110
			SD	60	80	60	50	20	110	3	40	20	0	3	3	330
	27	chl	Av.	210	60	150	170	80	340	10	20	6	1	3	2	16
			SD	80	30	60	70	30	140	4	10	3	1	1	1	9
KO33C	24	ill	Av.	70	190	420	70	40	140	7	290	60	2	4	14	2270
			SD	60	30	50	60	60	120	1	40	40	5	2	3	290
	23	chl	Av.	220	20	140	210	30	470	3	1	4	0	1	2	2
			SD	80	10	40	90	20	180	1	1	3	0	0	1	2
KO38	23	ill	Av.	80	190	490	90	20	140	10	280	80	2	3	15	2140
			SD	60	30	60	70	20	110	10	50	20	4	1	3	400
	19	chl	Av.	170	40	200	160	30	310	10	3	8	0	1	4	1
			SD	70	20	50	50	30	100	10	3	6	0	1	2	1
KO32A	13	cc	*Av.*	0.2	1.4	–	–	0.1	1.3	0.3	0.04	7700	–	–	0.06	3
			SD	0.1	0.7	–	–	0.1	0.7	0.1		1190	–	–	0.03	1
KO32B	14	cc	*Av.*	0.9	3	–	–	0.3	2	0.3	0.1	8150	–	–	0.1	6
			SD	0.8	2	–	–	0.3	1.8	0.1	0.03	1320	–	–	0.1	2
Hyuga Tectonic Mélange																
HN299A	46	ill	Av.	100	250	220	50	49	87	40	310	110	6	5	16	1080
			SD	60	50	50	40	27	52	30	50	390	9	2	4	210
	47	chl	Av.	230	60	120	80	23	180	13	40	20	3	3	4	50
			SD	90	40	30	30	11	68	7	30	50	4	1	2	20
	8	ab	Av.	–	54	30	–	24	–	14	40	150	4	2	3	120
			SD	–	5	10	–	11	–	5	20	80	4	1	2	90
HN299C	26	ill	Av.	70	240	180	160	320	80	290	310	80	20	5	18	1080
			SD	40	50	40	490	470	100	160	50	80	50	3	5	230
	21	chl	Av.	250	40	80	70	14	230	11	20	14	1	4	5	40
			SD	70	30	20	20	8	80	5	10	7	2	1	2	20
HN65	17	ill	Av.	140	260	230	20	30	50	11	320	80	7	5	21	980
			SD	80	70	40	10	20	30	7	60	60	8	2	7	190
	11	chl	Av.	440	130	100	20	17	50	7	150	12	5	3	7	280
			SD	360	50	30	20	8	30	4	40	6	9	1	2	100
Foliated Morotsuka																
HN145	52	ill	Av.	60	180	220	40	140	120	40	380	40	10	6	17	1340
			SD	20	70	20	20	80	60	30	20	10	20	3	4	100
	4	chl	Av.	80	80	110	110	370	380	20	–	–	3	4	–	–
			SD	40	40	30	50	170	190	10	–	–	4	2	–	–
HN243	29	ill	Av.	50	140	190	70	40	50	9	410	30	1	5	15	1280
			SD	20	70	60	30	20	50	4	110	10	0	2	5	370
	28	chl	Av.	120	70	110	70	50	290	20	8	3	1	3	3	5
			SD	50	20	30	30	30	130	10	5	2	1	1	2	3
HN285	35	ill	Av.	12	110	50	5	4	26	3	410	30	10	5	13	1340
			SD	2	10	20	2	2	4	1	20	10	13	1	2	110
	33	chl	Av.	140	7	80	110	50	510	8	2	3	0	1	1	6
			SD	20	5	10	30	30	70	9	2	1	0	0	1	2
NOB_23B	15	cc	*Av.*	0.5	1.6	–	–	0.5	2	0.4	0.3	4740	–	–	0.05	3
			SD	0.2	0.8	–	–	0.4	0.5	0.2	0.2	1530	–	–	0.02	1

concentrations of B, Na, K, Ca, Mg, Fe, Rb, Sr, Cs, and Ba in comparison to FI-poor zones (Fig. A.1). An example of which elements are found in the FIs is presented in form of box plots for FI-rich zones and adjacent FI-poor zones (Fig. 7).

Lithium, aluminum and titanium show no systematic difference between the two zones (Fig. 7). When ablating multiple FI instead of individual FI, subtracting the host mineral from the signal becomes challenging. Thus, Li, Al, and Ti are not generally considered for the fluid evolution studies due to inability to detect whether they are concentrated in the quartz crystal lattice or in both quartz and FIs.

For elements present in the FIs, element ratios on a mole basis are in the range of: Ca/Na – 0.06 to 13.23; B/Na – 0.02 to 0.57; K/Na – 0.01 to 5.69; Rb/Na – 2.2×10^{-5} to 0.05; Sr/Na – 0.0005 to 0.09; Ba/Na – 1.1×10^{-8} to 5.3×10^{-6}; and Cs/Na – 1.2×10^{-5} to 0.002 (Table 3). Sodium, calcium and potassium are major elements in FIs. Their concentrations have a large range: Na – 330 to 9700 μg/g; Ca – 360 to 10,800 μg/g; and

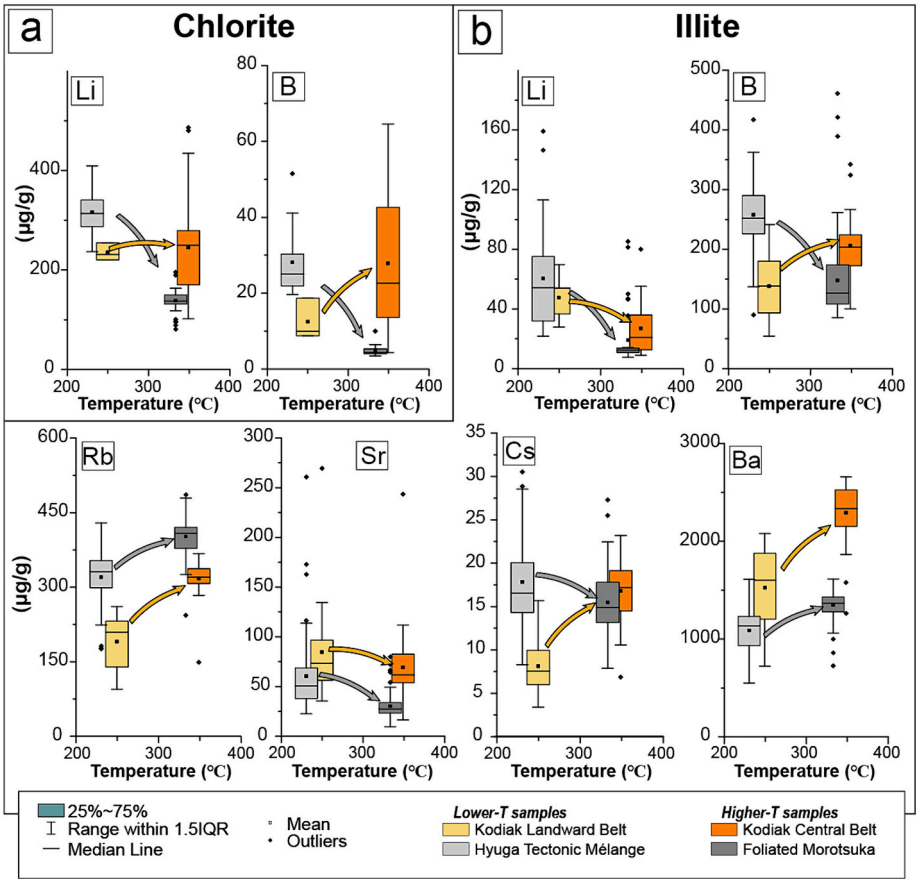

Fig. 6. Box plots of FME concentrations as a function of peak-metamorphic temperatures of (a) chlorite (Li and B) and (b) illite (Li, B, Rb, Sr, Cs and Ba), from the Kodiak complex and the Shimanto Belt, acquired by LA-ICP-MS. Arrows indicate the trend in chemical evolution of fluids as temperature rises, with orange representing Kodiak and gray representing Shimanto.

K – 10 to 10,600 μg/g (Table 3; Fig. 8). Potassium is the predominant cation in FIs of lower-grade veins, whereas Ca and Na have higher concentrations in FIs of higher-grade veins. Magnesium and iron are minor elements with ranges of 10 to 1200 μg/g and 20 to 1500 μg/g, respectively, with noticeably higher concentrations in higher-grade FIs (Fig. 8). The ranges of trace elements are: B – 4 to 870 μg/g; Rb – 0.4 to 40 μg/g; Sr – 10 to 380 μg/g; Cs – 0.1 to 12 μg/g; and Ba – 1 to 1800 μg/g. Trace elements show a narrower concentration range than major cations for the examined veins of each unit (Table 3; Fig. 8).

5. Discussion

5.1. Fluid-mobile elements redistribution in metasediments upon metamorphism

As mentioned in the § 1, the FME behavior is highly controlled by the geothermal gradient of the subduction zone, which in turn controls the occurrence of metamorphic reactions (e.g., Bebout et al., 2013). However, metasedimentary rocks from Kodiak and Shimanto display a similarly high geothermal gradient (20–30 °C/km) and a lack of major dehydration reactions in the range 230–350 °C (Rajič et al., 2023b). Despite experiencing similar peak pressure-temperature conditions and mineral reactions in both complexes, the FME behavior differs between two localities. Consequently, in order to elucidate the contrasting behavior of FME between Kodiak and Shimanto, alternative explanations must be considered.

5.1.1. FME budget in the solid matrix

In contrast to whole rock major element concentrations that do not vary when temperature increases from 230 to 350 °C (Rajič et al., 2023b), some of the FME concentrations vary across this temperature range (Fig. 5). In samples from the Kodiak complex, excluding the partial loss of cesium, all other FME are retained upon increasing temperature and the concentrations in higher-grade and the lower-grade samples are similar. Conversely, in the Shimanto Belt, FME show significant and systematic loss as temperature increases (Fig. 5). The different behaviors between the Kodiak complex and the Shimanto Belt can be illustrated by devolatilization indicators that have been extensively applied to other metasedimentary units (e.g., Bebout, 1995; Bebout et al., 2013), such as Rb/Cs or B/Li. Both Rb/Cs or B/Li are scattered among samples from the Kodiak complex, whereas in the Shimanto Belt Rb/Cs ratio increases and B/Li ratio systematically decreases (Fig. 9; Table 1). In terms of mineral reactions, the two opposing trends for FME budget can be accounted for by (i) changes in FME concentrations in the major minerals in the pelitic matrix, and (ii) mineral reactions and changes in phase proportions as a function of temperature (both phenomena being connected to the extent of fluid-rock interactions).

As noted by several studies, the FME budget in subducted lithologies is highly controlled by the abundance of phyllosilicates and their reactions during burial (e.g., Barnes et al., 2019a; Bebout et al., 1999, 2007, 2013; Busigny et al., 2003; Marschall et al., 2006). In the samples from this study, the main FME carriers are illite (boron, rubidium, barium, cesium ± lithium, strontium) and chlorite (lithium ± boron), with lower concentrations of LILE in albite (strontium ± rubidium, barium; Table 2; Fig. 10). Upon burial and increase in P and T, the minerals present in the pelitic matrix are affected by three main mineral reactions that affect their composition and/or abundance: illite

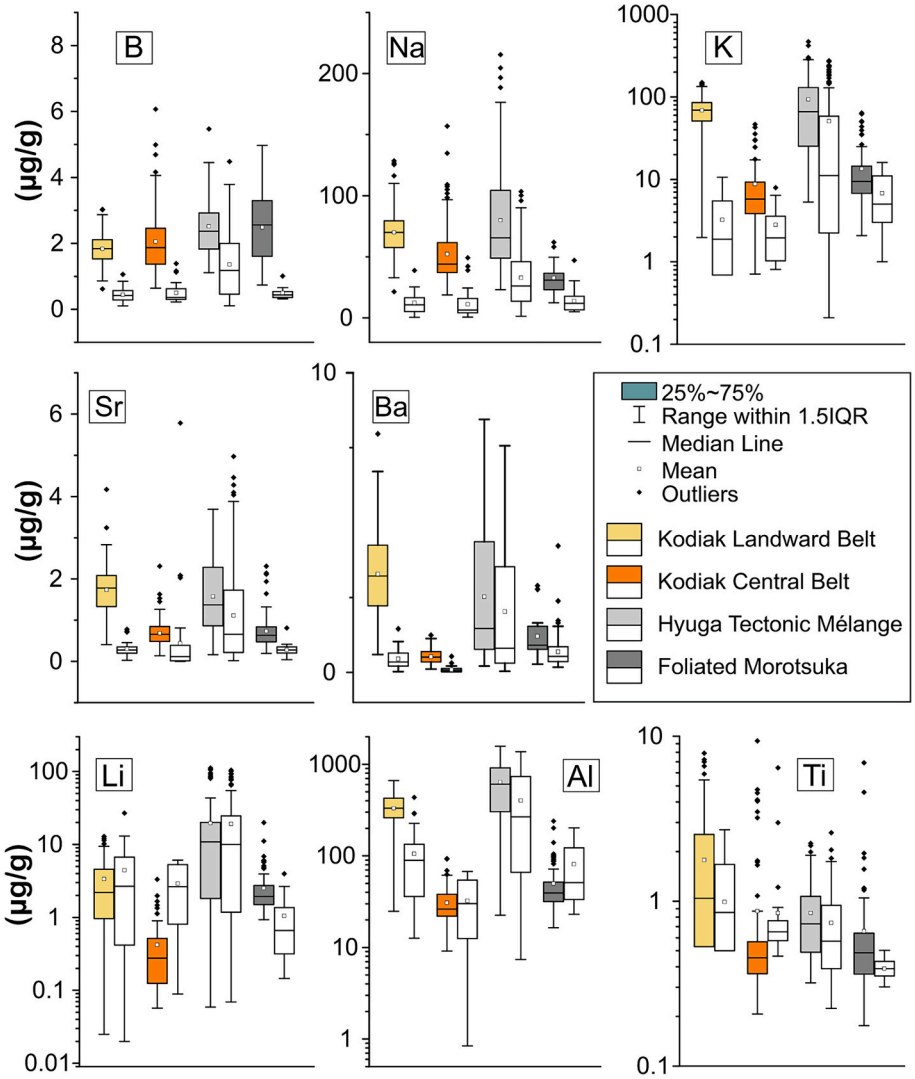

Fig. 7. The concentrations of B, Na, K, Sr, Ba, Li, Al, and Ti in quartz obtained with the LA-ICP-MS. For each unit, colored box plots correspond to the FI-rich quartz, whereas adjacent white box plots correspond to the FI-poor quartz. Note that FI-rich quartz is enriched in B, Na, K, Sr and Ba compared to FI-poor quartz, whereas measured concentrations of Li, Ti and Al are fairly equal in both zones.

recrystallization, chlorite crystallization and the dissolution of albite (Rajič et al., 2023b).

To examine the effects of these mineralogical reactions on FME budget, we performed mass balance calculations using the modal proportions of major minerals (XRD results; Rajič et al., 2023b) and the FME concentrations of each major mineral (Fig. 10). The calculated concentrations of lithium, rubidium, cesium, and barium are in good agreement (within ~20% difference) with whole-rock concentrations. In contrast, for boron and strontium, the calculated concentrations are systematically underestimated for most of samples (from ~25% to ~50% and from ~35% to ~75%, for B and Sr, respectively, see Fig. 10). The following discussion is therefore restricted to the elements for which the budget can be consistently estimated (Li, Rb, Cs and Ba), while B and Sr are discussed in § 5.1.2.

In the Kodiak complex, lithium concentration in chlorite, the main Li carrier, remains statistically identical as temperature increases (Fig. 6). Therefore, in spite of minor modal variations due to chlorite crystallization, the whole-rock stock of Li remains constant upon T increase (Fig. 5a). In contrast, in the Shimanto Belt, metamorphic illite and chlorite show significant depletion in lithium as temperature increases (Fig. 6), which result in the whole-rock decrease in Li upon T increase (Fig. 5a).

In both localities, recrystallized illite has higher concentrations of rubidium and barium in comparison to lower-grade illite (Fig. 6). As discussed in § 5.2, rubidium concentrations decrease in the fluid as temperature increases. Thus, newly formed illite consumes Rb from the fluid and possibly from dissolved fraction of albite. As a result, there are limited whole-rock variations in Ba and Rb concentrations upon T increase (Fig. 5c, e).

Finally, cesium shows contrasted behavior between the two geological examples. In Kodiak, similarly to Rb and Ba, cesium is retained in recrystallized illite and the whole-rock stock remains constant as temperature increases. In the Shimanto Belt example, cesium concentrations show slight decrease in illite as temperature increases, thus resulting in whole-rock decrease as well (Fig. 5f, 6).

In summary, in most cases (all elements for Kodiak, Rb and Ba for the Shimanto Belt), elements are redistributed between mineral phases upon temperature increase, without affecting the whole-rock budget. In contrast, Li and Cs are leached out of the rock in the Shimanto Belt example, as a result of a decreasing concentrations in newly formed minerals.

Consistent with the results of this study, Ramirez et al. (2021) described a similar depletion of FME in scaly fabrics (also known as pressure-solution seams) in metapelites of tectonic mélanges from the

Table 3
Average values and standard deviation of recovered concentrations of major, minor and trace elements in fluid inclusion populations and molal ratios for each studied formation. Only point analyses where Ca was successfully measured are reported.

	B	Na	Mg	K	Ca	Mn	Fe	Rb	Sr	Cs	Ba	B/Na	K/Na	Ca/Na	Rb/Na	Sr/Na	Cs/Na	Ba/Na
	μg/g	μg/g	μg/g	μg/g	μg/g	μg/g	μg/g	μg/g	μg/g	μg/g	μg/g	mole	mole	mole	mole	mole	mole	mole
Kodiak Landward Belt																		
Av.	110	4120	120	5550	1030	–	110	6	100	1	190	0.07	0.8	0.4	0.0004	0.008	4.09E-05	3.61E-07
SD	30	980	60	1600	1060	–	100	3	40	0.5	80	0.01	0.4	1.5	0.0003	0.009	2.08E-05	1.87E-07
Min	8	330	30	660	420	–	20	1	50	0.4	30							
Max	200	7040	350	9090	6640	–	390	14	190	2.5	360							
#	60	60	60	60	60	–	47	59	60	21	60							
Kodiak Central Belt																		
Av.	230	6060	210	1210	4540	30	170	3	80	3	60	0.11	0.2	0.6	0.0002	0.005	8.32E-05	8.04E-08
SD	100	1960	220	800	1710	20	130	2	30	1	30	0.04	0.1	0.5	0.0003	0.009	4.57E-05	4.31E-08
Min	60	1570	20	270	1800	5	60	1	10	1	10							
Max	490	9350	940	3560	9230	90	430	7	180	4	130							
#	32	32	32	32	32	26	17	25	32	30	32							
Hyuga Tectonic Mélange																		
Av.	120	2790	120	5630	1560	6	160	12.7	70	2	120	0.09	1.1	0.3	0.0012	0.006	1.16E-04	2.83E-07
SD	50	790	100	3040	910	4	100	8.1	40	1.1	90	0.04	1	0.2	0.0013	0.004	7.84E-05	2.67E-07
Min	30	1610	10	240	360	1	40	0.4	20	0.4	8							
Max	280	5560	400	10,260	4000	21	410	31.1	210	5.1	340							
#	36	36	36	36	36	34	27	36	36	36	36							
Foliated Morotsuka																		
Av.	273	3790	200	2200	6030	230	330	6.5	100	4.6	233	0.19	0.72	1.09	0.0011	0.007	0.0003	5.32E-07
SD	192	2070	240	2140	2490	360	370	7.4	60	3.1	428	0.08	2.86	1.99	0.0048	0.004	0.0002	8.60E-07
Min	4	50	10	10	980	2	60	0	20	0.1	1							
Max	865	9680	1240	10,650	10,780	1960	1520	38.9	380	11.9	1810							
#	62	62	62	62	62	61	40	61	62	62	62							

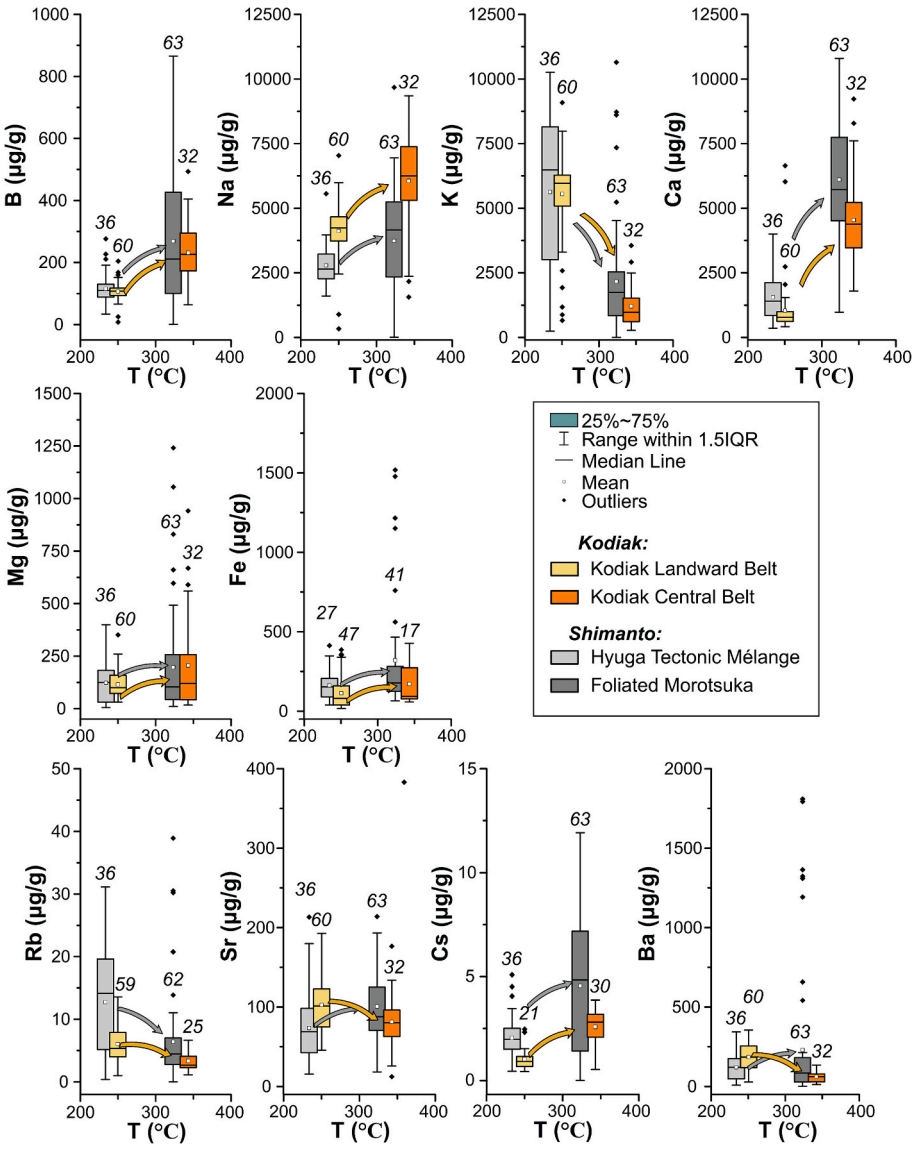

Fig. 8. Box plots illustrating recovered concentrations of fluid inclusions based on charge-balance approach (for B, Rb, Sr, Cs, Ba, Na, and K) plotted against peak-metamorphic temperatures. Arrows indicate the trend in chemical evolution of fluids as temperature rises, with orange representing Kodiak and gray representing Shimanto.

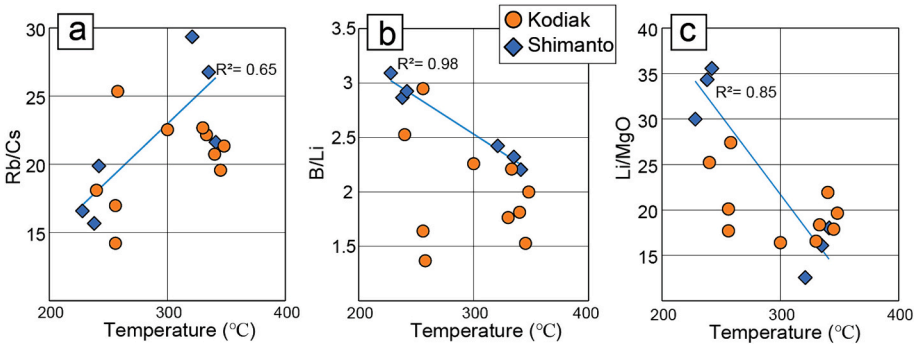

Fig. 9. (a) Rb/Cs, (b) B/Li and (c) Li/MgO ratios of metapelites from the Kodiak complex and the Shimanto Belt, plotted against peak-metamorphic temperatures.

Shimanto Belt and proposed that elements are remobilized by diffusion along grain boundaries into low, effective normal stress sites and incorporated into vein-forming minerals. However, vein-forming minerals (quartz and calcite) are small reservoirs for most FME, except for the limited incorporation of lithium in quartz (Raimbourg et al., 2021) or strontium in calcite (Table 2). Therefore, for most FME the whole-rock depletion implies that these elements are transferred into a fluid phase and leached out of the rock.

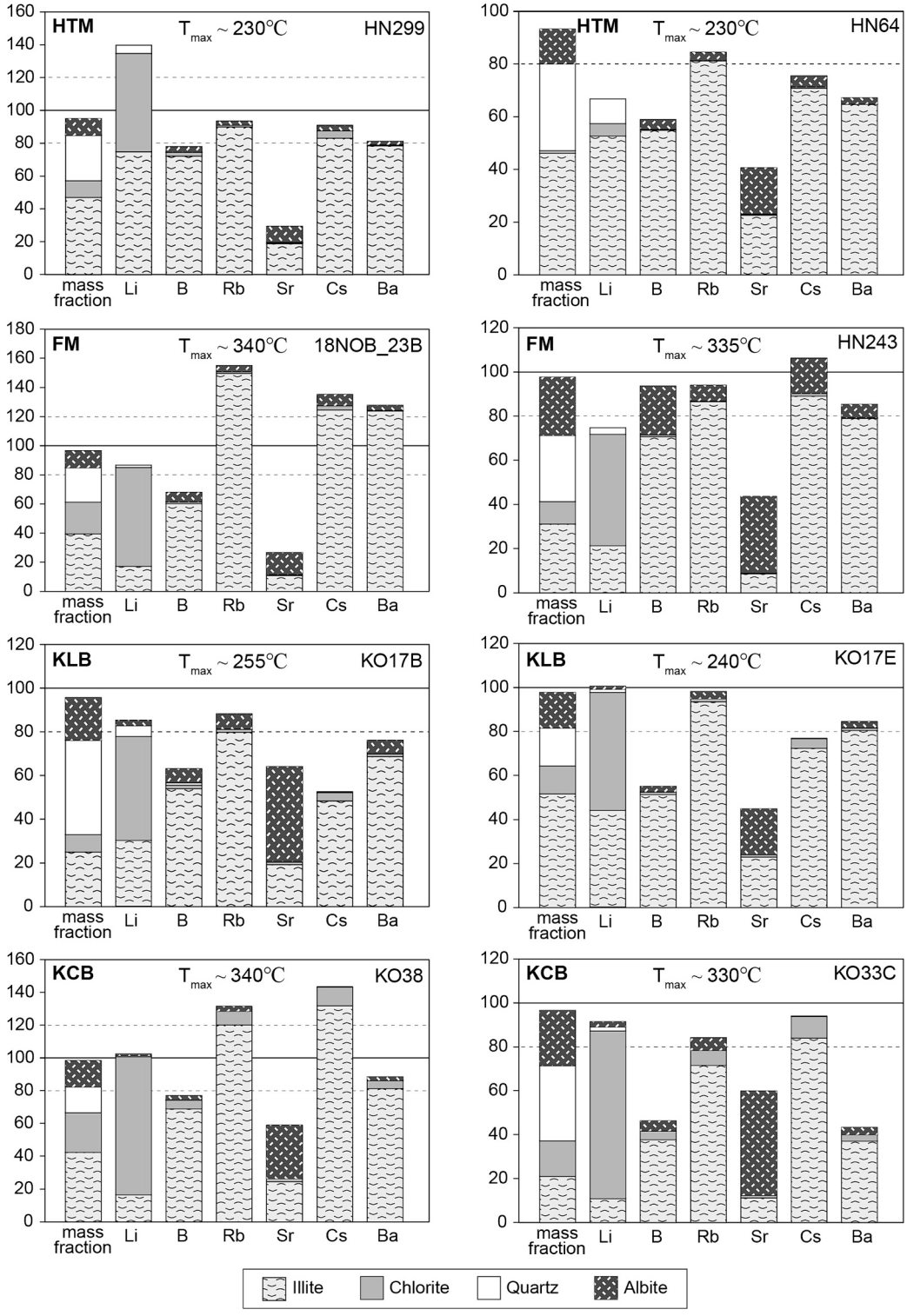

Fig. 10. Modal proportion of mineral phases and distribution of Li, B, Rb, Sr, Cs, and Ba among major mineral phases for selected samples from the Hyuga Tectonic Mélange (HTM), Foliated Morotsuka (FM), Kodiak Landward (KLB) and Central (KCB) Belts. The mass balance calculations of Li, B, Rb, Sr, Cs, and Ba were calculated from their concentrations in the major mineral phases (illite, chlorite, albite, and quartz) combined with XRD results (Rajič et al., 2023b) and normalized to 100% of whole-rock concentrations. Dashed lines represent 20% variations from the whole-rock concentrations.

5.1.2. Additional reservoirs for Sr and B

The mass balance calculations for strontium and boron are inconsistent with the whole-rock concentrations (Fig. 10). Strontium behaves similarly to calcium, and the presence of calcium-bearing phases, which may incorporate large amounts of strontium, can highly influence the strontium budget. In the examined samples, calcite is observed in the host rock as a minor phase. However, due to its very small grain size, FME concentrations of calcite in the pelitic matrix were not obtained and not considered in the mass balance calculations (Fig. 10). The modal fractions of calcite in the pelitic matrix range from ~0.5 to ~1.5% (Rajič et al., 2023b). Larger calcite crystals are observed in the veins (Rajič et al., 2023b) and have strontium concentrations of up to 1 wt%

(Table 2). If calcite in the pelitic matrix has similar strontium concentrations to the vein calcite (Table 2), it would correspond to 50–150 μg/g of strontium on the whole-rock scale, which resolves the strontium underestimation in mass balance calculations (Fig. 10). Thus, the underestimation of the whole-rock strontium budget is attributed to the omission of the minor proportion of calcite in the matrix from the mass balance calculation.

Regarding the discrepancy in boron, several possibilities can be raised, such as boron being stored in organic material (Williams et al., 2001b) or variable concentrations of B in illite as a function of grain size (Clauer et al., 2018; Clauer et al., 2014). First, although kerogen may contain significant boron concentrations (Williams et al., 2001b), the amount of carbonaceous material in metapelites is estimated to be ~0.5 wt% (Raimbourg et al., 2017) and therefore it is a second-order reservoir. Second, Clauer et al. (2018) pointed out that illitization progressed via dissolution-reprecipitation rather than by the solid-state substitution. As a consequence, newly precipitated illite is characterized by a larger grain size and lower boron concentrations than the older, smaller

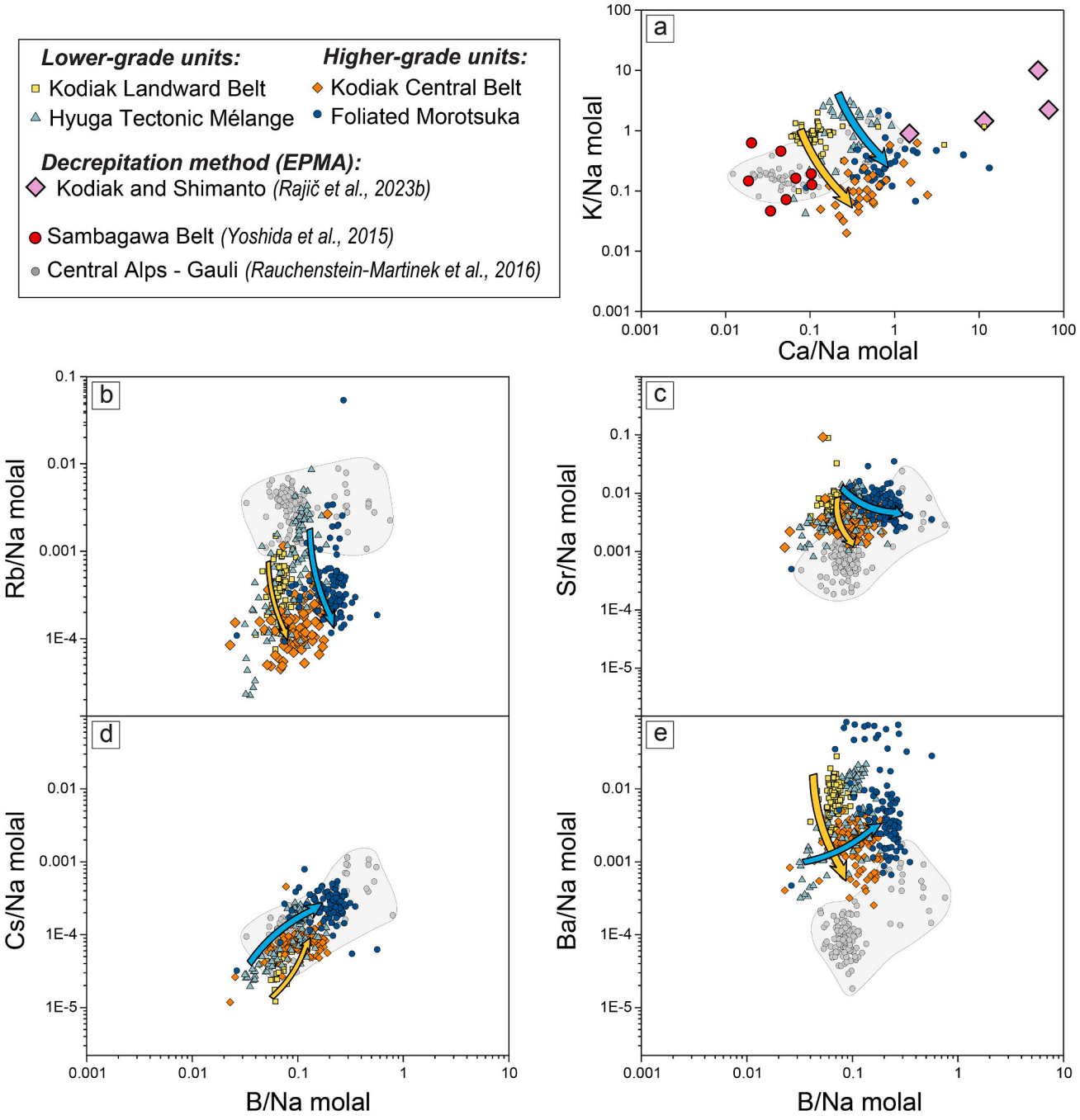

Fig. 11. (a) Ca/Na vs. K/Na molal ratios as well as (b) Rb/Na, (c) Sr/Na, (d) Cs/Na, and (e) Ba/Na molal ratios plotted against B/Na molal ratio of fluid inclusions, for each of studied formation. Arrows on the binary plots (orange – Kodiak; blue – Shimanto) represent the evolution of chemical composition as temperature rises. In (a), the pink points represent the average composition of all decrepitation mounds in individual samples of vein quartz from the Kodiak complex and the Shimanto Belt, acquired by EPMA (Rajič et al., 2023b). Gray areas represent fluid composition in metasedimentary units from the Central Alps (Gauli) determined by LA-ICP-MS on individual fluid inclusions (Rauchenstein-Martinek et al., 2016), whereas red points in (a) represent the chemical composition of fluid inclusions from the Sambagawa Belt determined by applying crush-leach technique (Yoshida et al., 2015). (For interpretation of the references to colour in this figure legend, the reader is referred to the web version of this article.)

grains (Clauer et al., 2018, Clauer et al., 2014). During this study, only sufficiently large grains (exceeding 30 μm in width) were analyzed by LA-ICP-MS (e.g. larger illite in the contact with the shear band shown in Fig. 3c); additionally, the FME concentration of smaller illite in the pelitic matrix was not measured. Therefore, the underestimation of the B content from individual mineral analyses (Fig. 10) could be explained by the grain size dependence of B concentration in illite.

In conclusion, we propose that strontium was remobilized by the fluid into dilatation sites, where it is stored in newly precipitated calcite. Regarding boron, the same general trend as Li can be observed. In the case of Kodiak, there is a slight increase in illite concentration in boron upon temperature increase. This increase, combined with the dissolution of albite (minor host of B), is consistent with the redistribution of B within the remaining illite population and constant whole-rock concentrations. In contrast, newly formed illite hosts lower proportion of B (Fig. 6) upon temperature increase in the case of Shimanto, consistent with a decrease in whole-rock concentration in B. Therefore, unlike the close-system behavior observed for Kodiak, the FME in high-temperature endmember in the Shimanto Belt was leached out by a circulating fluid.

5.2. Chemical evolution of the fluid and fluid-rock interaction

Bulk-microanalysis of FI populations revealed high variations in the major elements (sodium, potassium, and calcium) composition of the fluid (Figs. 7, 8). However, within a given geological unit, veins have similar chemical composition (Table 3; Fig. 11). Similar results were derived by using a decrepitation method for the same FIs (decrepitation of fluid inclusions occurs as a result of rapid thermal impact, where released material subsequently precipitates around the halos; Kontak, 2004): the proportion of sodium, potassium and calcium is highly variable and the majority of the analyzed evaporite mounds contained calcium as a major cation (Rajič et al., 2023b). All microprobe analyses in the decrepitation mounds show high variability; however, the average ratios in a single sample revealed similar K/Na and higher Ca/Na when compared to the results obtained by LA-ICP-MS (Fig. 11a). A discrepancy in Ca/Na ratios obtained by two methods can be explained by two reasons. First, derived Ca concentrations by LA-ICP-MS may be underestimated due to the analytical limitations as explained in § 3.2.2. Second, during the bulk microanalysis of FI population, multiple FIs were ablated, in contrast to individually analyzed evaporite mounds. This explains higher variability in EPMA point analyses when compared to LA-ICP-MS results, whereas the average composition of samples containing multiple mounds is similar to the LA-ICP-MS results (Fig. 11a).

To the best of our knowledge, other studies examining the chemical composition of FIs in subducted sediments that have experienced peak-temperatures of 230–350 °C are limited. The closest example are the higher-grade metasedimentary and metamafic units from the Sambagawa Belt, Japan, where crush-leach technique was applied to syn-metamorphic quartz veins (Yoshida et al., 2015). Their results in regard to K/Na, Ca/Na, and B/Na are consistent with those reported here (Fig. 11a). Another example are fissure veins from chlorite-mica schists in the Central Alps (Gauli), which have experienced sub-greenschist to amphibolite facies metamorphism (Rauchenstein-Martinek et al., 2016) and the chemical composition of individual FIs were measured by LA-ICP-MS (Fig. 11a-e). The absolute concentrations of major elements (sodium, potassium, and calcium) and trace elements (boron, strontium, cesium, and barium) are also in agreement with our results (Rauchenstein-Martinek et al., 2016; Table 3). Similarities in the determined fluid compositions of the two previous studies (Rauchenstein-Martinek et al., 2016; Yoshida et al., 2015) and the results from this study validate the approach of LA-ICP-MS bulk microanalysis of FI populations applied in this study (Fig. 11).

The ratios on a molal basis obtained in the present work, such as K/Na, Ca/Na, B/Na, Rb/Na, or Ba/Na are on average at least one order of magnitude higher than those of seawater and of the pore fluids of subducting sediments measured during IODP/ODP programs (Fig. 12). Only Cs/Na ratios are similar to the pore fluids (Fig. 12). This indicates that the fluids entrapped in FIs have chemical compositions that are significantly different from the initial pore fluid and that reflect the effect of diagenetic to low-grade metamorphic reactions. Upon burial of clay-rich sediments, the smectite-to-illite transformation is the critical mineral reaction that influences the evolution of the fluid, because smectite-illite contains boron, lithium, and LILE in both the interstitial site and the crystal structure. At temperatures >60 °C, alkali metals (Li, Na, K, and LILE) preferentially go into the fluid phase (Kastner et al., 2014; Seyfried et al., 1998; You and Gieskes, 2001). Most boron stored in clay minerals is released into the fluid phase at temperatures ~150 °C (Hüpers and Kopf, 2012; Williams et al., 2001a; You et al., 1995). Conversely, the depletion of potassium and rubidium in the fluid is expected when the transformation is completed, as illite incorporates higher concentrations of potassium and rubidium than smectite-illite (Kastner et al., 2014). Thus, major changes in the composition of pore fluids are likely to occur at temperatures <250 °C, with smaller compositional changes upon further temperature increase.

Nevertheless, upon a temperature increase from ~250 to ~350 °C, a few general geochemical trends are observed in veins from both the Kodiak complex and the Shimanto Belt: Ca/Na, B/Na, and Cs/Na ratios increase (Fig. 11a, d), whereas K/Na and Rb/Na ratios decrease as temperature increases (Fig. 11a, b). The Sr/Na ratio remains relatively constant. Only the Ba/Na ratio shows different trends between the two localities, with a slight decrease in the Kodiak complex and a slight increase in the Shimanto Belt with a temperature increase (Fig. 11e). These changes of element ratios as a function of temperature can be explained by examining the chemical evolution of the mineral phases and the mineral reactions in the pelitic matrix (Rajič et al., 2023b). For example, the K/Na ratio decreases as temperature increases because illite becomes more potassium-rich as temperature increases, and the fluid becomes enriched in sodium at higher temperatures related to the dissolution of albite in the pelitic matrix.

Furthermore, the fluid in higher-grade veins from both case studies is characterized by an enrichment in trace elements, and in both localities the increase in FME concentrations are similar (Fig. 8). In the Kodiak complex, there is no systematic loss of FME as temperature increases in the whole-rock (Fig. 5a-f). Conversely, in metapelites from Shimanto, FME show the most significant loss in whole-rock with increasing temperature (Fig. 5a-f). Thus, in both localities the same trends in the fluid were observed as temperature increased, whereas the whole-rock trends are opposite, and therefore the two case studies require different interpretations. The plausible explanations are (i) the difference in the size of fluid and rock reservoirs and (ii) the external influx of fluid in parallel to the observed metamorphic reactions responsible for release of FME from the rock.

5.2.1. Water-rock ratio

In order to explain the chemical evolution of pore fluids from 250 °C to 350 °C, the proportion of the solid and the fluid reservoirs needs to be considered. In metapelitic rocks at the depths >7 km the expected porosity is around 1–5 vol% or lower (Bray and Karig, 1985; Neuzil, 1994; Tsuji et al., 2006), meaning that the mass of pore fluid (for a fluid density of ~0.7 g/cm^3) is 70–330 times smaller than that of the solid in given mass of a solid (Fig. 13a). Thus, if the system is closed, minor changes in the FME concentrations of the solid caused by interaction with a fluid should have significant impact on the fluid composition. This may be the case in the Kodiak complex, as no significant loss of FME is observed from the solid with increasing temperature (Fig. 5), whereas FIs record an enrichment in FME, especially for boron and cesium (Fig. 8).

In the Kodiak complex, the theoretical mass solid/fluid ratios were combined with measured concentrations of element i in the initial solid $\left(c_i^{s,0}\right)$, initial fluid $\left(c_i^{F,0}\right)$ and final fluid $\left(c_i^{F,f}\right)$, allowing for concentra-

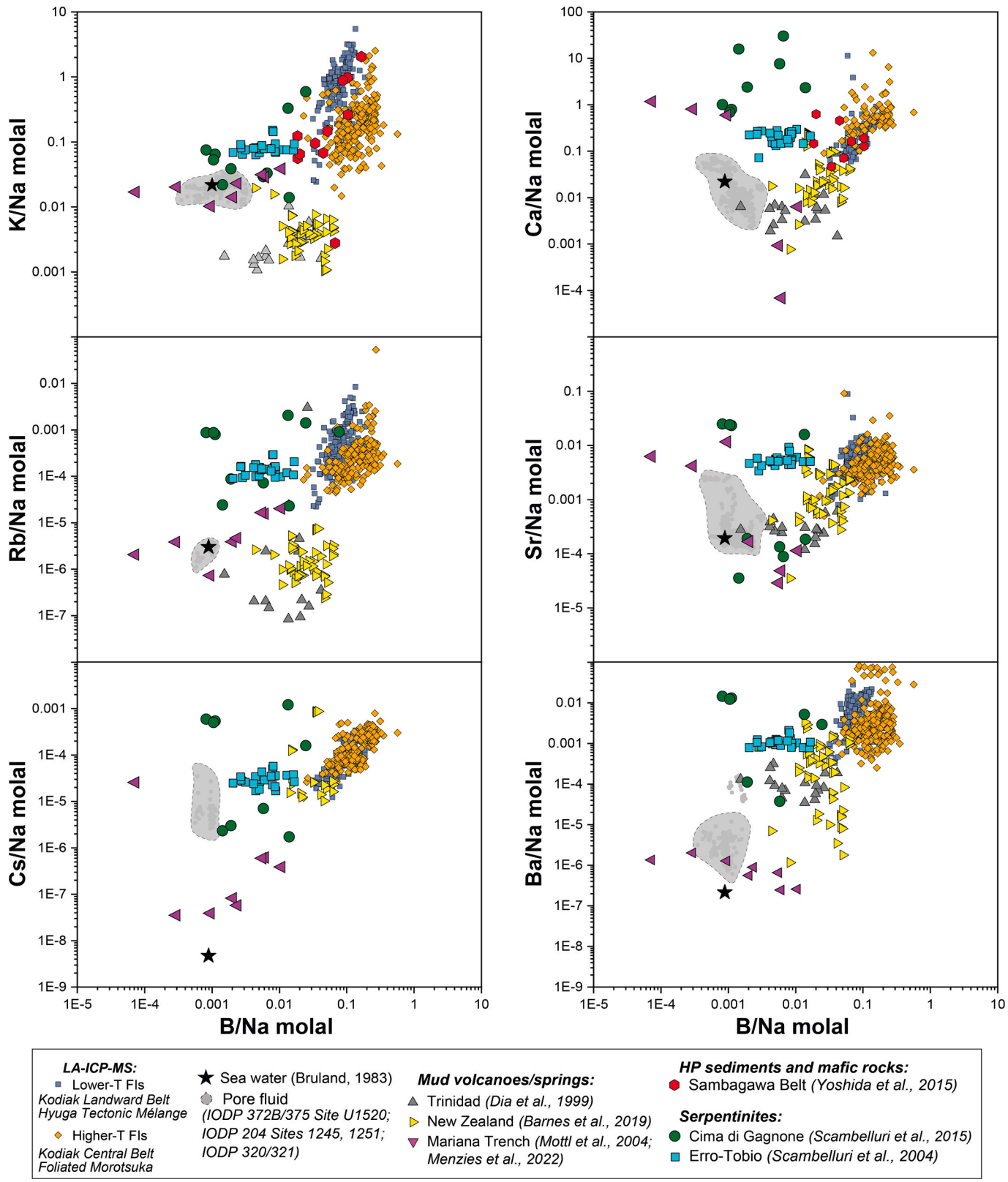

Fig. 12. Binary plots of B/Na vs. K/Na, Ca/Na, Rb/Na, Sr/Na, Cs/Na, and Ba/Na molal ratios of fluid inclusions examined in this study by LA-ICP-MS, with the compilation of possible fluid reservoirs involved into chemical evolution of subduction zone fluids in sedimentary units: The seawater composition (Bruland, 1983); The chemistry of pore fluid: IODP 372B/375 Site U1520 (Wallace et al., 2019); IODP 204 Sites 1245 and 1251 (Tréhu et al., 2003); IODP 320/321 (Pälike et al., 2009); Mud volcanoes and hot/cold springs (Barnes et al., 2019b; Dia et al., 1999); Crush-leach results from the Sambagawa Belt (Yoshida et al., 2015); Fluids released during dehydration reactions in serpentinites (Scambelluri et al., 2004a, 2015); Serpentinite mud volcano fluids from the Mariana Forearc (Hulme et al., 2010; Menzies et al., 2022; Mottl et al., 2004).

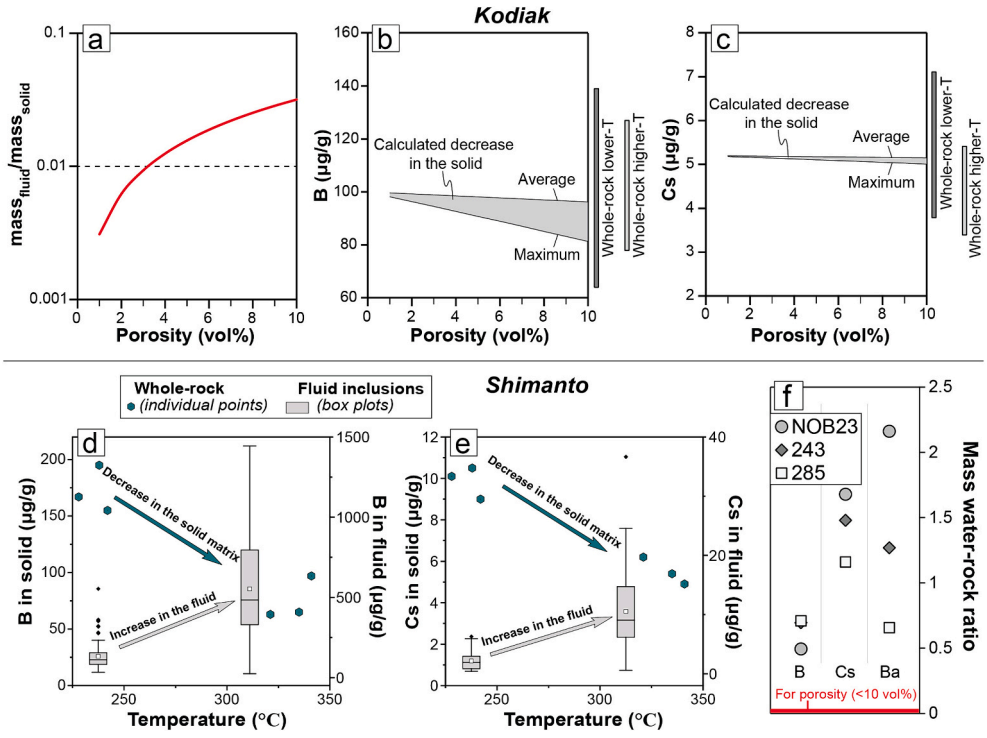

Fig. 13. The mass fluid-rock ratio calculations for the Kodiak complex and the Shimanto Belt. (a) The mass fluid-rock ratio as a function of the porosity, showing that the fluid reservoir is significantly lower than the solid. Calculations of required decrease in concentrations of (b) B and (c) Cs from the solid in the Kodiak complex, in order to create the measured enrichment of B and Cs in the pore fluid. Adjacent box plots represent the range of measured whole-rock concentrations of boron and cesium in lower- and higher-temperature samples. (d) Boron and (e) cesium concentrations decrease at whole-rock scale (primary y-axis) as a function of temperature in the Shimanto Belt, whereas the fluid shows an enrichment (secondary y-axis). (f) Mass water-rock ratios calculated for boron, cesium, and barium. Red area represents water-rock ratio to the porosity of <10 vol% in the case of closed system. (For interpretation of the references to colour in this figure legend, the reader is referred to the web version of this article.)

tions in the final solid $\left(c_i^{S,f}\right)$ to be calculated (Eq. 6). In order to cause an enrichment in boron concentrations in the fluid (from ~110 µg/g to 230–700 µg/g; Table 4), the boron concentration in the solid is required to decrease from ~100 µg/g to ~91 µg/g (Fig. 13b), which represents a < 10% decrease (assuming a porosity of 1–5 vol%). For cesium, in order to increase concentrations in the fluid from ~1 µg/g to 3–7 µg/g, the cesium concentrations in the solid is required to decrease from 5.2 µg/g to 5.1 µg/g (Fig. 13c), which is <2%. Therefore, because of the small volume of the pore fluid reservoir (compared to the solid matrix), the concentration of FME is much more sensitive to rock/fluid exchanges than the solid matrix.

Conversely, in the case of Shimanto, significantly higher amounts of FME are released from the solid (Fig. 13d, e) and therefore the fluid should be drastically enriched in all released elements. However, the enrichment is on the same order as in the fluids from the Kodiak complex (Fig. 8). Thus, another mechanism should be considered, such as the percolation of externally derived fluids, which are responsible for decrease in concentrations of FME in the solid. In order to calculate the required mass of fluid to leach the FME from the solid, the mass water-rock ratio is calculated following eq. (6). Calculated mass water-rock ratios in the Shimanto Belt range from 0.5 to 0.7, 1.2 to 1.7, and 0.7 to 2.2 for boron, cesium, and barium, respectively (Fig. 13f).

5.2.2. Closed vs. open system

Derived mass water-rock ratios in the Foliated Morotsuka (Shimanto Belt) are ~30 to ~130 times higher than expected if the system was closed and characterized by porosity lower than 5 vol% (Fig. 13f). This implies that a large flux of fluid percolated through the rocks and leached the elements out of the minerals. Two factors can be invoked to explain why fluid percolation was present at Shimanto Belt and was not observed at Kodiak. The first is the large amount of strain the rocks experienced in the Foliated Morotsuka (Raimbourg et al., 2014), where the pervasive network of shear zones greatly enhanced rock permeability (Cox, 2002, 2010; Wibberley and Shimamoto, 2003). The second is the proximity of large-scale fault zones, which may have acted as pathways for deeper and overpressurized fluid to drive fluid-rock interactions (Faulkner et al., 2010, Faulkner et al., 2003; Herviou and Bonnet, 2023; Saffer and Tobin, 2011). The Foliated Morotsuka is located in the hanging wall of a large-scale fault zone, the Nobeoka Tectonic Line (Kondo et al., 2005), which may have promoted percolation of external fluid through these rocks. For these reasons, we propose that high water-rock ratios in the Foliated Morotsuka are the result of fluid flow from deeper levels that was focused on the structural horizon where strain is the highest. Similar observations have been reported for the Glarus Thrust in the Eastern Helvetic Alps (Abart et al., 2002; Badertscher et al., 2002; Burkhard et al., 1992; Burkhard and Kerrich, 1988; Hürzeler and Abart, 2008). Another crucial observation is that some samples (e.g., HN145) collected from the Foliated Morotsuka are located at substantial distance from the Nobeoka Tectonic Line (see Fig. 1b). This significant distance from the NTL implies a substantial damage zone influenced by the infiltration of fluids originating from the deeper regions of the subduction zone.

In the case of the Kodiak Central Belt, textural evidence around crack-seal veins is consistent with local migration of SiO_2 due to pore-fluid diffusion of SiO_2 from the pelitic matrix (Fisher and Brantley, 1992; Rajič et al., 2023b) and there is a lack of evidence to support long-distance transport (Fisher et al., 1995; Fisher and Brantley, 2014). In contrast to the Foliated Morotsuka, the Kodiak Central Belt is located in the central part of large turbiditic sequence far from any recognized large-scale faults (Fig. 1).

In the Kodiak complex, trace elements behaved similarly to major

elements (Rajič et al., 2023b): The system was closed at the large (typically >hundreds of meters or kilometers) scale and open at the centimeter scale, where FME were transported from the pelitic matrix towards the vein and the newly formed minerals (illite and chlorite) in contact with the vein (Fig. 14). Conversely, there is a discrepancy between the behavior of major and trace elements during prograde metamorphism in the Shimanto Belt. No systematic changes have been reported for major elements in HTM and FM, which indicates a closed system (Rajič et al., 2023b). However, fluid-mobile elements examined during this study show a systematic decrease as temperature increases, requiring high mass water-rock ratio to leach these elements out of the rocks.

Thus, we propose that the contrasting behavior between the closed system (with respect to FME) observed in the Alaskan terranes and the open system observed in the Japanese terranes is the result of their internal strain and their proximity to large-scale faults, which concentrated the fluid flow (Fig. 14).

5.3. Implications for fluid circulation in subduction zones

This study shows that boron and cesium are the most sensitive tracers of fluid-mediated processes in subduction zones, which is consistent with previous use of boron and cesium as tracers for prograde dehydration of altered oceanic crust (Angiboust et al., 2014; Bebout, 1991; Bebout et al., 1993, 2007; Lafay et al., 2013; Marschall et al., 2006; Moran et al., 1992) or serpentinites (Deschamps et al., 2010, 2011, 2013; Hattori and Guillot, 2007; Lafay et al., 2013; Li and Lee, 2006; Scambelluri et al., 2004a, 2004b). Furthermore, derived water-rock ratios suggest that high quantities of fluid circulated through the Foliated Morotsuka, where such fluids may be expelled through the subduction zone forearc along permeable horizons. Additionally, despite the absence of dehydration reactions within analyzed samples from the Shimanto Belt (Rajič et al., 2023b), there is a noticeable loss of FME. This observation is consistent with the high sensitivity of the FME not just to water loss, but also to the volume of fluids traversing through rocks. Consequently, assesing the FME evolution of both the solid and the fluid has a great potential to characterize rocks undergoing substantial fluid influx, such as metasomatic rocks formed along the subduction interface (Angiboust et al., 2014; Penniston-Dorland and Harvey, 2023).

In addition, similarities are observed between boron and cesium concentrations (or B/Na and Cs/Na ratios) in FIs acquired during this study and the chemical composition of mud volcano fluids from Trinidad (Dia et al., 1999) or hot and cold springs from New Zealand (Barnes et al., 2019b). The origin of spring fluids from New Zealand have been interpreted to be derived from dehydrated subducted sediments based on high $\delta^{18}O$ and δD values in fluids flowing through the springs (Barnes et al., 2019b; Giggenbach et al., 1993; Reyes et al., 2010). The fluids from mud volcanoes and springs (Dia et al., 1999; Barnes et al., 2019b) are characterized by a composition that is between that of the seawater and fluids from this study (Fig. 12), confirming the mixing of seawater that is percolating downwards and metamorphic fluids that are percolating upwards, as proposed for the Hikurangi accretionary prism (Reyes et al., 2010). Our study further confirms that compositionally altered pore fluids escaped from subducting plate and travel along zones with high permeability back to the seafloor.

However, the fluid composition preserved in FIs examined in this study closely resembles the potential fluid sources found in deeply subducted lithologies. In this context, the fluid that traverses the Foliated Morotsuka may originate from any of the H_2O-bearing lithologies that were subducted to significant depths, including sediments, altered oceanic crust or serpentinites. The major dehydration reactions in these lithologies and subsequent release of water occurs deeper than the depths at which the units from this study were buried (Aizawa et al., 1999; Deschamps et al., 2013; John et al., 2011; Kameda et al., 2017; Peacock, 1993; Scambelluri et al., 2004b; Zack et al., 2003). When comparing the fluid compositions reported in this study with that of metasedimentary and metamafic units from the Sambagawa Belt (subducted to depths between 15 and 60 km; Yoshida et al., 2015), the fluid composition is relatively similar (Fig. 12). Dehydration reactions in altered oceanic crust may also contribute to the upwelling fluids. A good example of a release of such fluids from altered oceanic crust at temperatures <300 °C are serpentinite mud volcano fluids from the Mariana forearc (Hulme et al., 2010; Menzies et al., 2022; Mottl et al., 2004). However, serpentinite mud volcano fluids exhibit a composition similar to seawater (Fig. 12), implying their limited relevance in this study. Another significant source of fluids are serpentinites, with the major dehydration reactions occurring at depths between 40 and 60 km (Scambelluri et al., 2004a, 2015). Upon comparing the chemical composition of fluid from this study with those released during major dehydration reactions in serpentinites (Scambelluri et al., 2004a, 2015), only slight depletion in boron relative to our results is observed (Fig. 12). Therefore, gaining a better understanding of which subducted lithology and which specific reaction primarily contribute to the fluids percolating through the Foliated Morotsuka requires further investigation.

6. Conclusions

This study provides an insight into the behavior of fluid-mobile elements by examining whole-rock concentrations, concentrations in individual minerals, and fluid inclusions from syn-subduction veins in the Kodiak complex, Alaska and the Shimanto Belt, Japan. The Kodiak complex exhibits closed system behavior and retention of all FME at temperatures between ~230 and ~350 °C. This retention reflects the redistribution of the FME between major mineral phases in the pelitic matrix. The Shimanto Belt exhibits open system behavior and significant loss is observed for all FME at temperatures between ~230 °C and ~350 °C, except for barium and rubidium for which the variations are much more limited. In the Shimanto Belt strontium is transfered to calcite in the veins, whereas there is a release of lithium, boron, cesium, and potentially minor proportion of barium into the fluid.

The fluid inclusions hosted in quartz in metasedimentary rocks that experienced temperatures 230–350 °C from the two localities show identical trends of evolution with temperature, such as increase in boron and cesium. In the Kodiak complex, the enrichment in boron and cesium in the fluid from ~230 °C to ~350 °C is consistent with a very small loss of boron and cesium from the solid, below that which can be detected by whole-rock analysis. In the Shimanto Belt, the significant FME loss is observed as temperature rises, which is consistent with a decrease in FME concentrations in the solid by a percolating fluid and water-rock ratios ranging between 0.5 and 2.2. These high water-rock ratios are at least one order of magnitude larger than the in situ pore fluid. The difference between the closed (Kodiak) and open (Shimanto) system behavior is attributed to the variation in the amount of internal strain (controlling premeability) and the distance to large-scale faults (draining fluids).

Furthermore, recovered chemical composition of these fluids have FME concentrations are at least an order of magnitude higher than that of interstitial pore fluid in shallow sediments or seawater. Similarities in composition between FIs trapped in metamorphic veins and mud volcano fluids or springs in subduction zone forearcs are consistent with the contribution of fluids being expelled from sedimentary units forming the seismogenic plate interface along permeable zones through the subduction zone forearc.

Supplementary data to this article can be found online at https://doi.org/10.1016/j.chemgeo.2024.122141

CRediT authorship contribution statement

Kristijan Rajič: Writing – original draft, Software, Methodology, Investigation, Formal analysis, Data curation, Conceptualization. **Hugues Raimbourg:** Writing – review & editing, Visualization,

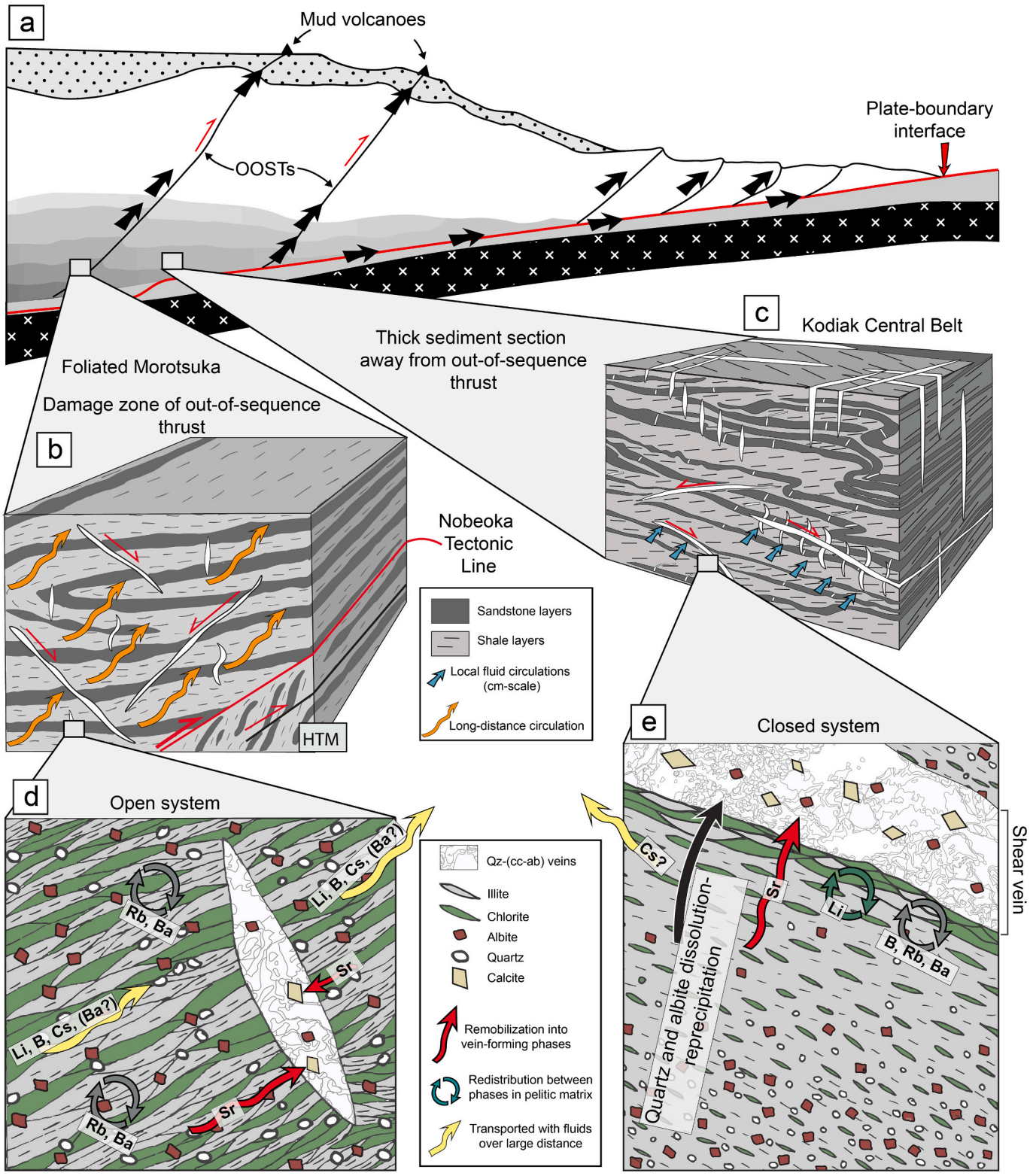

Fig. 14. The schematic scenario of FME budget evolution at studied sites, from the location within the wedge down to thin section: (a) A sketch of an accretionary wedge redrawn after Kastner et al. (2014) with the relative locations of studied units, the Foliated Morotsuka and the Kodiak Central Belt. The Foliated Morotsuka is located in the hanging wall of the out-of-sequence thrust (Nobeoka Tectonic Line), whereas the Kodiak Central Belt was underplated in the middle of thick turbiditic sequence far from any large-scale faults. A 3D sketch of (b) the Foliated Morotsuka and (c) the Kodiak Central Belt with presented deformation structures and possible scenarios for fluid flow. (d) and (e) show details of the mineralogy of metapelites from both localities and their influence on FME budget. In the Foliated Morotsuka (d), Li, B, Cs, and ± Ba are leached from the host rock, with only Sr stored in vein-forming calcite. Conversely, in the Kodiak Central Belt (e), Li, B, Rb, and Ba are reorganized between illite, chlorite and albite and Sr being stored in the vein calcite. Only a small proportion of Cs is potentially lost to the fluid.

Supervision, Resources, Project administration, Methodology, Funding acquisition, Conceptualization. **Austin M. Gion:** Writing – review & editing, Visualization, Software, Methodology, Data curation, Conceptualization. **Catherine Lerouge:** Supervision. **Saskia Erdmann:** Writing – review & editing, Methodology, Investigation, Formal analysis, Data curation.

Declaration of competing interest

The authors declare that they have no known competing financial interests or personal relationships that could have appeared to influence the work reported in this paper.

Data availability

Supplementary data are available through Zenodo repository at https://doi.org/10.5281/zenodo.10658679 or online at https://doi.org/10.1016/j.chemgeo.2024.122141.

Acknowledgments

The authors acknowledge support from LabEx VOLTAIRE (ANR-10-LABX-100-01) and EquipEx PLANEX (ANR-11-EQPX-0036) projects. We thank S. Janiec for the preparation of thin sections. S. Agostini and three anonymous reviewers are thanked for thoughtful comments and suggestions that improved the manuscript. We thank as well C. Romano for editorial handling.

References

Abart, R., Badertscher, N., Burkhard, M., Povoden, E., 2002. Oxygen, carbon and strontium isotope systematics in two profiles across the Glarus thrust: implications for fluid flow. Contrib. Mineral. Petrol. 143, 192–208. https://doi.org/10.1007/s00410-001-0326-5.

Aizawa, Y., Tatsumi, Y., Yamada, H., 1999. Element transport by dehydration of subducted sediments: Implication for arc and ocean island magmatism. Island Arc 8, 38–46. https://doi.org/10.1046/j.1440-1738.1999.00217.x.

Allan, M.M., Yardley, B.W.D., Forbes, L.J., Shmulovich, K.I., Banks, D.A., Shepherd, T.J., 2005. Validation of LA-ICP-MS fluid inclusion analysis with synthetic fluid inclusions. Am. Mineral. 90, 1767–1775. https://doi.org/10.2138/am.2005.1822.

Angiboust, S., Pettke, T., De Hoog, J.C.M., Caron, B., Oncken, O., 2014. Channelized Fluid Flow and Eclogite-facies Metasomatism along the Subduction Shear Zone. J. Petrol. 55, 883–916. https://doi.org/10.1093/petrology/egu010.

Audet, P., Schwartz, S.Y., 2013. Hydrologic control of forearc strength and seismicity in the Costa Rican subduction zone. Nat. Geosci. 6, 852–855. https://doi.org/10.1038/ngeo1927.

Badertscher, N.P., Beaudoin, G., Therrien, R., Burkhard, M., 2002. Glarus overthrust: a major pathway for the escape of fluids out of the Alpine orogen. Geol 30, 875–878. https://doi.org/10.1130/0091-7613(2002)030<0875:GOAMPF>2.0.CO;2.

Bangs, N.L., Shipley, T.H., Moore, G.F., 1996. Elevated fluid pressure and fault zone dilation inferred from seismic models of the northern Barbados Ridge decollement. J. Geophys. Res. 101, 627–642. https://doi.org/10.1029/95JB02402.

Bangs, N.L.B., Shipley, T.H., Moore, J.C., Moore, G.F., 1999. Fluid accumulation and channeling along the northern Barbados Ridge decollement thrust. J. Geophys. Res. 104, 20399–20414. https://doi.org/10.1029/1999JB900133.

Barnes, J.D., Cullen, J., Barker, S., Agostini, S., Penniston-Dorland, S., Lassiter, J.C., Klügel, A., Wallace, L., 2019a. The role of the upper plate in controlling fluid-mobile element (Cl, Li, B) cycling through subduction zones: Hikurangi forearc, New Zealand. Geosphere 15, 642–658. https://doi.org/10.1130/GES02057.1.

Barnes, J.D., Penniston-Dorland, S.C., Bebout, G.E., Hoover, W., Beaudoin, G.M., Agard, P., 2019b. Chlorine and lithium behavior in metasedimentary rocks during prograde metamorphism: a comparative study of exhumed subduction complexes (Catalina Schist and Schistes Lustrés). Lithos 336–337, 40–53. https://doi.org/10.1016/j.lithos.2019.03.028.

Bebout, G.E., 1991. Field-based evidence for Devolatilization in Subduction zones: Implications for Arc Magmatism. Science, New Series 251, 413–416.

Bebout, G.E., 1995. The impact of subduction-zone metamorphism on mantle-ocean chemical cycling. Chem. Geol. 126, 191–218. https://doi.org/10.1016/0009-2541(95)00118-5.

Bebout, G.E., 2007. Metamorphic chemical geodynamics of subduction zones. Earth Planet. Sci. Lett. 260, 373–393.

Bebout, G.E., 2014. Basic Considerations: Sampling, the Key for a Successful Applied Geochemical Survey for Mineral Exploration and Environmental Purposes. In: Treatise on Geochemistry. Elsevier, pp. 703–747. https://doi.org/10.1016/B978-0-08-095975-7.01401-7.

Bebout, G.E., 2021. Insights Into Subduction Zone Dynamics. In: Encyclopedia of Geology. Elsevier, pp. 233–247. https://doi.org/10.1016/B978-0-08-102908-4.00150-8.

Bebout, G.E., Ryan, J.G., Leeman, W.P., 1993. B⊠be systematics in subduction-related metamorphic rocks: Characterization of the subducted component. Geochim. Cosmochim. Acta 57, 2227–2237. https://doi.org/10.1016/0016-7037(93)90565-E.

Bebout, G.E., Ryan, J.G., Leeman, W.P., Bebout, A.E., 1999. Fractionation of trace elements by subduction-zone metamorphism — effect of convergent-margin thermal evolution. Earth Planet. Sci. Lett. 171, 63–81. https://doi.org/10.1016/S0012-821X(99)00135-1.

Bebout, G.E., Bebout, A.E., Graham, C.M., 2007. Cycling of B, Li, and LILE (K, Cs, Rb, Ba, Sr) into subduction zones: SIMS evidence from micas in high-P/T metasedimentary rocks. Chem. Geol. 239, 284–304. https://doi.org/10.1016/j.chemgeo.2006.10.016.

Bebout, G.E., Agard, P., Kobayashi, K., Moriguti, T., Nakamura, E., 2013. Devolatilization history and trace element mobility in deeply subducted sedimentary rocks: Evidence from Western Alps HP/UHP suites. Chem. Geol. 342, 1–20. https://doi.org/10.1016/j.chemgeo.2013.01.009.

Behr, W.M., Bürgmann, R., 2021. What's down there? The structures, materials and environment of deep-seated slow slip and tremor. Phil. Trans. R. Soc. A 379, 20200218. https://doi.org/10.1098/rsta.2020.0218.

Bekaert, D.V., Turner, S.J., Broadley, M.W., Barnes, J.D., Halldórsson, S.A., Labidi, J., Wade, J., Walowski, K.J., Barry, P.H., 2020. Subduction-Driven Volatile Recycling: a Global Mass Balance. Annu. Rev. Earth Planet. Sci. 49, 37–70.

Bray, C.J., Karig, D.E., 1985. Porosity of sediments in accretionary prisms and some implications for dewatering processes. J. Geophys. Res. 90, 768–778. https://doi.org/10.1029/JB090iB01p00768.

Bruland, K.W., 1983. Trace elements in Sea-water. In: Chemical Oceanography. Elsevier, pp. 157–220. https://doi.org/10.1016/B978-0-12-588608-6.50009-2.

Burkhard, M., Kerrich, R., 1988. Fluid regimes in the deformation of the Helvetic nappes, Switzerland, as inferred from stable isotope data. Contrib. Mineral. Petrol. 99, 416–429.

Burkhard, M., Kerrich, R., Maas, R., Fyfe, W.S., 1992. Stable and Sr-isotope evidence for fluid advection during thrusting of the Glarus nappe (swiss alps). Contrib. Mineral. Petrol. 112, 293–311. https://doi.org/10.1007/BF00310462.

Busigny, V., Cartigny, P., Philippot, P., Ader, M., Javoy, M., 2003. Massive recycling of nitrogen and other fluid-mobile elements (K, Rb, Cs, H) in a cold slab environment: evidence from HP to UHP oceanic metasediments of the Schistes Lustrés nappe (western Alps, Europe). Earth Planet. Sci. Lett. 215, 27–42. https://doi.org/10.1016/S0012-821X(03)00453-9.

Byrne, T., Fisher, D.M., 1987. Episodic growth of the Kodiak convergent margin. Nature 325, 338–341.

Chan, L.-H., Kastner, M., 2000. Lithium isotopic compositions of pore fuids and sediments in the Costa Rica subduction zone: implications for £uid processes and sediment contribution to the arc volcanoes. Earth Planet. Sci. Lett. 183, 275–290.

Clauer, N., Honty, M., Fallick, A.E., Šucha, V., Aubert, A., 2014. Regional illitization in bentonite beds from the East Slovak Basin based on isotopic characteristics (K-Ar, δ ^{18}O and δD) of illite-type nanoparticles. Clay Miner. 49, 247–275. https://doi.org/10.1180/claymin.2014.049.2.07.

Clauer, N., Williams, L.B., Lemarchand, D., Florian, P., Honty, M., 2018. Illitization decrypted by B and Li isotope geochemistry of nanometer-sized illite crystals from bentonite beds, East Slovak Basin. Chem. Geol. 477, 177–194. https://doi.org/10.1016/j.chemgeo.2017.10.027.

Connelly, W., 1978. Uyak complex, Kodiak Islands, Alaska: a cretaceous subduction complex. Geol. Soc. Am. Bull. 89, 755–769.

Cox, S.F., 2002. Fluid flow in mid-to deep crustal shear systems: Experimental constraints, observations on exhumed high fluid flux shear systems, and implications for seismogenic processes. Earth Planet Sp 54, 1121–1125. https://doi.org/10.1186/BF03353312.

Cox, S.F., 2010. The application of failure mode diagrams for exploring the roles of fluid pressure and stress states in controlling styles of fracture-controlled permeability enhancement in faults and shear zones. Geofluids 10, 217–233. https://doi.org/10.1111/j.1468-8123.2010.00281.x.

Deschamps, F., Guillot, S., Godard, M., Chauvel, C., Andreani, M., Hattori, K., 2010. In situ characterization of serpentinites from forearc mantle wedges: timing of serpentinization and behavior of fluid-mobile elements in subduction zones. Chem. Geol. 269, 262–277. https://doi.org/10.1016/j.chemgeo.2009.10.002.

Deschamps, F., Guillot, S., Godard, M., Andreani, M., Hattori, K., 2011. Serpentinites act as sponges for fluid-mobile elements in abyssal and subduction zone environments: Serpentinites act as sponges for fluid-mobile elements. Terra Nova 23, 171–178. https://doi.org/10.1111/j.1365-3121.2011.00995.x.

Deschamps, F., Godard, M., Guillot, S., Hattori, K., 2013. Geochemistry of subduction zone serpentinites: a review. Lithos 178, 96–127. https://doi.org/10.1016/j.lithos.2013.05.019.

Dia, A.N., Castrec-Rouelle, M., Boulègue, J., Comeau, P., 1999. Trinidad mud volcanoes: where do the expelled fluids come from? Geochim. Cosmochim. Acta 63, 1023–1038. https://doi.org/10.1016/S0016-7037(98)00309-3.

Dimitrov, L.I., 2002. Mud volcanoes—the most important pathway for degassing deeply buried sediments. Earth Sci. Rev. 59, 49–76. https://doi.org/10.1016/S0012-8252(02)00069-7.

Ditullio, L., Byrne, T., 1990. Deformation paths in the shallow levels of an accretionary prism: the Eocene Shimanto belt of Southwest Japan. Geol. Soc. Am. Bull. 102, 1420–1438. https://doi.org/10.1130/0016-7606(1990)102<1420:DPITSL>2.3.CO;2.

Dragovic, B., Samanta, L.M., Baxter, E.F., Selverstone, J., 2012. Using garnet to constrain the duration and rate of water-releasing metamorphic reactions during subduction: an example from Sifnos, Greece. Chem. Geol. 314, 9–22.

Faulkner, D.R., Lewis, A.C., Rutter, E.H., 2003. On the internal structure and mechanics of large strike-slip fault zones: field observations of the Carboneras fault in southeastern Spain. Tectonophysics 367, 235–251. https://doi.org/10.1016/S0040-1951(03)00134-3.

Faulkner, D.R., Jackson, C.A.L., Lunn, R.J., Schlische, R.W., Shipton, Z.K., Wibberley, C. A.J., Withjack, M.O., 2010. A review of recent developments concerning the structure, mechanics and fluid flow properties of fault zones. J. Struct. Geol. 32, 1557–1575. https://doi.org/10.1016/j.jsg.2010.06.009.

Fisher, D.M., Brantley, S.L., 1992. Models of quartz overgrowth and vein formation: Deformation and episodic fluid flow in an ancient subduction zone. J. Geophys. Res. 97, 20043–20061. https://doi.org/10.1029/92JB01582.

Fisher, D.M., Brantley, S.L., 2014. The role of silica redistribution in the evolution of slip instabilities along subduction interfaces: Constraints from the Kodiak accretionary complex, Alaska. J. Struct. Geol. 69, 395–414. https://doi.org/10.1016/j.jsg.2014.03.010.

Fisher, D., Byrne, T., 1987. Structural evolution of underthrusted sediments, Kodiak Islands, Alaska. Tectonics 6, 775–793. https://doi.org/10.1029/TC006i006p00775.

Fisher, D.M., Brantley, S.L., Everett, M., Dzvonik, J., 1995. Cyclic fluid flow through a regionally extensive fracture network within the Kodiak accretionary prism. J. Geophys. Res. 100, 12881–12894. https://doi.org/10.1029/94JB02816.

Giggenbach, W.F., Sano, Y., Wakita, H., 1993. Isotopic composition of helium, and CO2 and CH4 contents in gases produced along the New Zealand part of a convergent plate boundary. Geochim. Cosmochim. Acta 57, 3427–3455. https://doi.org/10.1016/0016-7037(93)90549-C.

Hacker, B.R., 2008. H2O subduction beyond arcs. Geochem. Geophys. Geosyst. 9 https://doi.org/10.1029/2007GC001707 n/a-n/a.

Hacker, B.R., Abers, G.A., Peacock, S.M., 2003. Subduction factory 1. Theoretical mineralogy, densities, seismic wave speeds, and H $_2$ O contents. J. Geophys. Res. 108 https://doi.org/10.1029/2001JB001127.

Hattori, K.H., Guillot, S., 2007. Geochemical character of serpentinites associated with high- to ultrahigh-pressure metamorphic rocks in the Alps, Cuba, and the Himalayas: Recycling of elements in subduction zones: GEOCHEMISTRY OF SERPENTINITES. Geochem. Geophys. Geosyst. 8 https://doi.org/10.1029/2007GC001594 n/a-n/a.

Herviou, C., Bonnet, G., 2023. Paleocene-Eocene High-Pressure Carbonation of Western Alps Serpentinites: Positive Feedback between Deformation and CO2-CH4 Fluid Ingression Responsible for Slab Slicing? Geochemistry, Geophysics, Geosystems.

Herviou, C., Verlaguet, A., Agard, P., Locatelli, M., Raimbourg, H., Lefeuvre, B., Dubacq, B., 2021. Along-dip variations of subduction fluids: the 30–80 km depth traverse of the Schistes Lustrés complex (Queyras-Monviso, W. Alps). Lithos 394–395, 106168. https://doi.org/10.1016/j.lithos.2021.106168.

Hoover, W.F., Penniston-Dorland, S., Baumgartner, L., Bouvier, A.-S., Dragovic, B., Locatelli, M., Angiboust, S., Agard, P., 2022. Episodic fluid flow in an eclogite-facies shear zone: Insights from Li isotope zoning in garnet. Geology 50, 746–750. https://doi.org/10.1130/G49737.1.

Hulme, S.M., Wheat, C.G., Fryer, P., Mottl, M.J., 2010. Pore water chemistry of the mariana serpentinite mud volcanoes: a window to the seismogenic zone. Geochem. Geophys. Geosyst. 11 https://doi.org/10.1029/2009GC002674.

Hüpers, A., Kopf, A.J., 2012. Effect of smectite dehydration on pore water geochemistry in the shallow subduction zone: an experimental approach. Geochem. Geophys. Geosyst. 13 https://doi.org/10.1029/2012GC004212.

Hürzeler, J.-P., Abart, R., 2008. Fluid flow and rock alteration along the Glarus thrust. Swiss J. Geosci. 101, 251–268. https://doi.org/10.1007/s00015-008-1265-1.

Ishikawa, T., Tanimizu, M., Nagaishi, K., Matsuoka, J., Tadai, O., Sakaguchi, M., Hirono, T., Mishima, T., Tanikawa, W., Lin, W., Kikuta, H., Soh, W., Song, S.-R., 2008. Coseismic fluid–rock interactions at high temperatures in the Chelungpu fault. Nat. Geosci. 1, 679–683. https://doi.org/10.1038/ngeo308.

John, T., Scambelluri, M., Frische, M., Barnes, J.D., Bach, W., 2011. Dehydration of subducting serpentinite: Implications for halogen mobility in subduction zones and the deep halogen cycle. Earth Planet. Sci. Lett. 308, 65–76. https://doi.org/10.1016/j.epsl.2011.05.038.

Kameda, J., Raimbourg, H., Kogure, T., Kimura, G., 2011. Low-grade metamorphism around the down-dip limit of seismogenic subduction zones: example from an ancient accretionary complex in the Shimanto Belt, Japan. Tectonophysics 502, 383–392. https://doi.org/10.1016/j.tecto.2011.02.010.

Kameda, J., Inoue, S., Tanikawa, W., Yamaguchi, A., Hamada, Y., Hashimoto, Y., Kimura, G., 2017. Alteration and dehydration of subducting oceanic crust within subduction zones: implications for décollement step-down and plate-boundary seismogenesis. Earth Planets Space 69, 52. https://doi.org/10.1186/s40623-017-0635-1.

Kastner, M., Solomon, E.A., Harris, R.N., Torres, M.E., 2014. Fluid Origins, Thermal Regimes, and Fluid and Solute Fluxes in the Forearc of Subduction Zones. In: Developments in Marine Geology. Elsevier, pp. 671–733. https://doi.org/10.1016/B978-0-444-62617-2.00022-0.

Kerrick, D.M., Connolly, J.A.D., 2001. Metamorphic devolatilization of subducted marine sediments and the transport of volatiles into the Earth's mantle. Nature 411, 293–296. https://doi.org/10.1038/35077056.

Kominz, M.A., Pekar, S.F., 2001. Oligocene eustasy from two-dimensional sequence stratigraphic backstripping. Geol. Soc. Am. Bull. 113, 291–304. https://doi.org/10.1130/0016-7606(2001)113<0291:OEFTDS>2.0.CO;2.

Kondo, H., Kimura, G., Masago, H., Ohmori-Ikehara, K., Kitamura, Y., Ikesawa, E., Sakaguchi, A., Yamaguchi, A., Okamoto, S., 2005. Deformation and fluid flow of a major out-of-sequence thrust located at seismogenic depth in an accretionary complex: Nobeoka Thrust in the Shimanto Belt, Kyushu, Japan: NOBEOKA THRUST, a SEISMOGENIC OST. Tectonics 24. https://doi.org/10.1029/2004TC001655 n/a-n/a.

Lafay, R., Deschamps, F., Schwartz, S., Guillot, S., Godard, M., Debret, B., Nicollet, C., 2013. High-pressure serpentinites, a trap-and-release system controlled by metamorphic conditions: example from the Piedmont zone of the western Alps. Chem. Geol. 343, 38–54. https://doi.org/10.1016/j.chemgeo.2013.02.008.

Lauer, R.M., Saffer, D.M., 2012. Fluid budgets of subduction zone forearcs: The contribution of splay faults: SPLAY FAULTS AND FOREARC HYDROGEOLOGY. Geophys. Res. Lett. 39, n/a-n/a. doi:https://doi.org/10.1029/2012GL052182.

Lauer, R.M., Saffer, D.M., 2015. The impact of splay faults on fluid flow, solute transport, and pore pressure distribution in subduction zones: a case study offshore the Nicoya Peninsula, Costa Rica: Splay faults and forearc fluid flow. Geochem. Geophys. Geosyst. 16, 1089–1104. https://doi.org/10.1002/2014GC005638.

Li, Z.-X.A., Lee, C.-T.A., 2006. Geochemical investigation of serpentinized oceanic lithospheric mantle in the Feather River Ophiolite, California: Implications for the recycling rate of water by subduction. Chem. Geol. 235, 161–185. https://doi.org/10.1016/j.chemgeo.2006.06.011.

Mackenzie, J.S., 1989. Geochemical study of the greenstones of the cretaceous and Paleogene Shimanto accretionary complex in eastern Kyushu: Implications for origin and mode of emplacement. J. Mineral. Petrol. Econ. Geol. 84, 278–292. https://doi.org/10.2465/ganko.84.278.

Marschall, H.R., Altherr, R., Ludwig, T., Kalt, A., Gméling, K., Kasztovszky, Z., 2006. Partitioning and budget of Li, be and B in high-pressure metamorphic rocks. Geochim. Cosmochim. Acta 70, 4750–4769. https://doi.org/10.1016/j.gca.2006.07.006.

Martin, J.B., Kastner, M., Henry, P., Le Pichon, X., Lallement, S., 1996. Chemical and isotopic evidence for sources of fluids in a mud volcano field seaward of the Barbados accretionary wedge. J. Geophys. Res. 101, 20325–20345. https://doi.org/10.1029/96JB00140.

Menzies, C.D., Price, R.E., Ryan, J., Sissmann, O., Takai, K., Wheat, C.G., 2022. Spatial variation of subduction zone fluids during progressive subduction: insights from Serpentinite Mud Volcanoes. Geochim. Cosmochim. Acta 319, 118–134. https://doi.org/10.1016/j.gca.2021.10.030.

Moore, J.C., Byrne, T., Plumley, P.W., Reid, M., Gibbons, H., Coe, R.S., 1983. Paleogene evolution of the Kodiak 266 Islands, Alaska: Consequences of ridge-trench interaction in a more southerly latitude. Tectonics 2, 265–293.

Moore, G.F., Taira, A., Klaus, A., Becker, L., Boeckel, B., Cragg, B.A., Dean, A., Fergusson, C.L., Henry, P., Hirano, S., Hisamitsu, T., Hunze, S., Kastner, M., Maltman, A.J., Morgan, J.K., Murakami, Y., Saffer, D.M., Sánchez-Gómez, M., Screaton, E.J., Smith, D.C., Spivack, A.J., Steurer, J., Tobin, H.J., Ujiie, K., Underwood, M.B., Wilson, M., 2001. New insights into deformation and fluid flow processes in the Nankai Trough accretionary prism: Results of Ocean Drilling Program Leg 190: DEFORMATION AND FLUID FLOW PROCESSES. Geochem. Geophys. Geosyst. 2 https://doi.org/10.1029/2001GC000166 n/a-n/a.

Moran, A.E., Sisson, V.B., Leeman, W.P., 1992. Boron depletion during progressive metamorphism: Implications for subduction processes. Earth Planet. Sci. Lett. 111, 331–349. https://doi.org/10.1016/0012-821X(92)90188-2.

Mottl, M.J., Wheat, C.G., Fryer, P., Gharib, J., Martin, J.B., 2004. Chemistry of springs across the Mariana forearcshows progressive devolatilization of the subducting slab. Geochim. Cosmochim. Acta 68 (23), 4915–4933. https://doi.org/10.1016/j.gca.2004.05.037.

Muñoz-Montecinos, J., Angiboust, S., Garcia-Casco, A., Glodny, J., Bebout, G., 2021. Episodic hydrofracturing and large-scale flushing along deep subduction interfaces: Implications for fluid transfer and carbon recycling (Zagros Orogen, southeastern Iran). Chem. Geol. 571, 120173. https://doi.org/10.1016/j.chemgeo.2021.120173.

Neuzil, C.E., 1994. How permeable are clays and shales? Water Resour. Res. 30, 145–150.

Oleskevich, D.A., Hyndman, R.D., Wang, K., 1999. The updip and downdip limits to great subduction earthquakes: Thermal and structural models of Cascadia, south Alaska, SW Japan, and Chile. J. Geophys. Res. 104 (B7), 14965–14991. https://doi.org/10.1029/1999JB900060.

Palazzin, G., Raimbourg, H., Famin, V., Jolivet, L., Kusaba, Y., Yamaguchi, A., 2016. Deformation processes at the down-dip limit of the seismogenic zone: the example of Shimanto accretionary complex. Tectonophysics 687, 28–43. https://doi.org/10.1016/j.tecto.2016.08.013.

Pälike, H., Nishi, H., Lyle, M., et al., 2009. Expedition 320/321 scientists. Pac. Equatorial Transect IODP Prel Rept. 320 https://doi.org/10.2204/iodp.pr.320.2009.

Peacock, S.M., 1993. The importance of blueschist → eclogite dehydration reactions in subducting oceanic crust. Geol. Soc. Am. Bull. 105, 684–694. https://doi.org/10.1130/0016-7606(1993)105<0684:TIOBED>2.3.CO;2.

Penniston-Dorland, S.C., Harvey, K.M., 2023. Constraints on tectonic processes in subduction mélange: A review of insights from the Catalina Schist (CA, USA). Geosyst. Geoenviron. 2, 100190. https://doi.org/10.1016/j.geogeo.2023.100190.

Peters, D., Bretscher, A., John, T., Scambelluri, M., Pettke, T., 2017. Fluid-mobile elements in serpentinites: Constraints on serpentinisation environments and element cycling in subduction zones. Chem. Geol. 466, 654–666. https://doi.org/10.1016/j.chemgeo.2017.07.017.

Plafker, G., Moore, J.C., Winkler, G.R., Berg, H., 1994. Geology of the southern Alaska margin. The geology of 249 Alaska: Boulder, Colorado. Geological Society of America, Geology of North America 1, 389–449.

Raimbourg, H., Tadahiro, S., Asuka, Y., Haruka, Y., Kimura, G., 2009. Horizontal shortening versus vertical loading in accretionary prisms. Geochem. Geophys. Geosyst. 10 https://doi.org/10.1029/2008GC002279 n/a-n/a.

Raimbourg, H., Augier, R., Famin, V., Gadenne, L., Palazzin, G., Yamaguchi, A., Kimura, G., 2014. Long-term evolution of an accretionary prism: the case study of the Shimanto Belt, Kyushu, Japan: long-term evolution of the Shimanto Belt. Tectonics 33, 936–959. https://doi.org/10.1002/2013TC003412.

Raimbourg, H., Thiéry, R., Vacelet, M., Famin, V., Ramboz, C., Boussafir, M., Disnar, J.-R., Yamaguchi, A., 2017. Organic matter cracking: a source of fluid overpressure in subducting sediments. Tectonophysics 721, 254–274. https://doi.org/10.1016/j.tecto.2017.08.005.

Raimbourg, H., Famin, V., Palazzin, G., Mayoux, M., Jolivet, L., Ramboz, C., Yamaguchi, A., 2018. Fluid properties and dynamics along the seismogenic plate interface. Geosphere 14, 469–491. https://doi.org/10.1130/GES01504.1.

Raimbourg, H., Rajič, K., Moris-Muttoni, B., Famin, V., Palazzin, G., Fisher, D.M., Morell, K., Erdmann, S., Di Carlo, I., Montmartin, C., 2021. Quartz vein geochemistry records deformation processes in convergent zones. Geochem. Geophys. Geosyst. 22 https://doi.org/10.1029/2020GC009201.

Rajič, K., Raimbourg, H., Famin, V., Moris-Muttoni, B., Fisher, D.M., Morell, K.D., Canizarés, A., 2023a. Exhuming an Accretionary Prism: a Case Study of the Kodiak Accretionary complex, Alaska, USA. Tectonics 42. https://doi.org/10.1029/2023TC007754 e2023TC007754.

Rajič, K., Raimbourg, H., Lerouge, C., Famin, V., Dubacq, B., Canizarès, A., Di Carlo, I., Maubec, N., 2023b. Metamorphic reactions and their implication for the fluid budget in metapelites at seismogenic depths in subduction zones. Tectonophysics 857.

Ramirez, G., Smye, A., Fisher, D.M., Hashimoto, Y., Yamaguchi, A., 2021. Constraints on Element Mobility during Deformation within the Seismogenic Zone, Shimanto Belt, Japan. Geochem. Geophys. Geosyst. 22 https://doi.org/10.1029/2020GC009594.

Rauchenstein-Martinek, K., Wagner, T., Wälle, M., Heinrich, C.A., Arlt, T., 2016. Chemical evolution of metamorphic fluids in the Central Alps, Switzerland: insight from LA-ICPMS analysis of fluid inclusions. Geofluids 16, 877–908. https://doi.org/10.1111/gfl.12194.

Rea, D.K., Ruff, L.J., 1996. Composition and mass flux of sediment entering the world's subduction zones: Implications for global sediment budgets, great earthquakes, and volcanism. Earth Planet. Sci. Lett. 140, 1–12. https://doi.org/10.1016/0012-821X(96)00036-2.

Reyes, A.G., Christenson, B.W., Faure, K., 2010. Sources of solutes and heat in low-enthalpy mineral waters and their relation to tectonic setting, New Zealand. J. Volcanol. Geotherm. Res. 192, 117–141. https://doi.org/10.1016/j.jvolgeores.2010.02.015.

Reynard, B., 2013. Serpentine in active subduction zones. Lithos 178, 171–185. https://doi.org/10.1016/j.lithos.2012.10.012.

Rowe, C.D., Meneghini, F., Moore, J.C., 2009. Fluid-rich damage zone of an ancient out-of-sequence thrust, Kodiak Islands, Alaska. Tectonics 28. https://doi.org/10.1029/2007TC002126 n/a-n/a.

Rupke, L., 2004. Serpentine and the subduction zone water cycle. Earth Planet. Sci. Lett. 223, 17–34. https://doi.org/10.1016/j.epsl.2004.04.018.

Saffer, D.M., Tobin, H.J., 2011. Hydrogeology and Mechanics of Subduction Zone Forearcs: Fluid Flow and Pore pressure. Annu. Rev. Earth Planet. Sci. 39, 157–186. https://doi.org/10.1146/annurev-earth-040610-133408.

Sample, J.C., Fisher, D.M., 1986. Duplex accretion and underplating in an ancient accretionary prism, Kodiak Islands, Alaska. Geology 14, 160–163.

Sample, J.C., Moore, J.C., 1987. Structural style and kinematics of an underplated slate belt, Kodiak and adjacent 260 islands, Alaska. Geol. Soc. Am. Bull. 99, 7–20.

Scambelluri, M., Fiebig, J., Malaspina, N., Müntener, O., Pettke, T., 2004a. Serpentinite Subduction: Implications for Fluid Processes and Trace-Element Recycling. Int. Geol. Rev. 46, 595–613. https://doi.org/10.2747/0020-6814.46.7.595.

Scambelluri, M., Müntener, O., Ottolini, L., Pettke, T.T., Vannucci, R., 2004b. The fate of B, Cl and Li in the subducted oceanic mantle and in the antigorite breakdown fluids. Earth Planet. Sci. Lett. 222, 217–234. https://doi.org/10.1016/j.epsl.2004.02.012.

Scambelluri, M., Pettke, T., Cannaò, E., 2015. Fluid-related inclusions in Alpine high-pressure peridotite reveal trace element recycling during subduction-zone dehydration of serpentinized mantle (Cima di Gagnone, Swiss Alps). Earth Planet. Sci. Lett. 429, 45–59. https://doi.org/10.1016/j.epsl.2015.07.060.

Scambelluri, M., Cannaò, E., Gilio, M., 2019. The water and fluid-mobile element cycles during serpentinite subduction. A review. Eur. J. Mineral. 31, 405–428. https://doi.org/10.1127/ejm/2019/0031-2842.

Schmidt, M.W., Poli, S., 2014. Devolatilization During Subduction. In: Treatise on Geochemistry. Elsevier, pp. 669–701. https://doi.org/10.1016/B978-0-08-095975-7.00321-1.

Seyfried, W.E., Chen, X., Chan, L.H., 1998. Trace element mobility and lithum exchange during hydrothermal alteration of seafloor weatherd basalt; an experimental study at 350 degrees C, 500 bars. Ceochim. Cosmochim. Acta 62, 949–960.

Shervais, J.W., Jean, M.M., 2012. Inside the subduction factory: Modeling fluid mobile element enrichment in the mantle wedge above a subduction zone. Geochim. Cosmochim. Acta 95, 270–285. https://doi.org/10.1016/j.gca.2012.07.006.

Stern, C.R., 2011. Subduction erosion: rates, mechanisms, and its role in arc magmatism and the evolution of the continental crust and mantle. Gondwana Res. 20, 284–308. https://doi.org/10.1016/j.gr.2011.03.006.

Taira, A., Okada, H., Whitaker, J.H., Smith, A.J., 1982. The Shimanto Belt of Japan: Cretaceous-lower Miocene active-margin sedimentation. Geol. Soc. Lond. Spec. Publ. 10, 5–26. https://doi.org/10.1144/GSL.SP.1982.010.01.01.

Tatsumi, Y., Kogiso, T., 2003. The subduction factory: its role in the evolution of the Earth's crust and mantle. SP 219, 55–80. https://doi.org/10.1144/GSL.SP.2003.219.01.03.

Tenthorey, E., Hermann, J., 2004. Composition of fluids during serpentinite breakdown in subduction zones: evidence for limited boron mobility. Geol 32, 865. https://doi.org/10.1130/G20610.1.

Tobin, H., Vannucchi, P., Meschede, M., 2001. Structure, inferred mechanical properties, and implications for fluid transport in the décollement zone, Costa Rica convergent margin. Geol 29, 907. https://doi.org/10.1130/0091-7613(2001)029<0907:SIMPAI>2.0.CO;2.

Toriumi, M., Teruya, J., 1988. Tectono-metamorphism of the Shimanto Belt. Mod. Geol. 12, 303–324.

Tréhu, A.M., Bohrmann, G., Rack, F.R., Torres, M.E., Bangs, N.L., Barr, S.R., Borowski, W.S., Tréhu, A.M., Bohrmann, G., Rack, F.R., Torres, M.E., et al., 2003. Shipboard Scientific Party. In: Proc. ODP, Init. Repts., 204 Ocean Drilling Program, College Station, TX, pp. 1–131.

Tsuji, T., Kimura, G., Okamoto, S., Kono, F., Mochinaga, H., Saeki, T., Tokuyama, H., 2006. Modern and ancient seismogenic out-of-sequence thrusts in the Nankai accretionary prism: Comparison of laboratory-derived physical properties and seismic reflection data: MODERN AND ANCIENT SEISMOGENIC THRUSTS. Geophys. Res. Lett. 33 https://doi.org/10.1029/2006GL027025 n/a-n/a.

Tuba, G., Kontak, D.J., Zajacz, Z., Petrus, J.A., 2019. Bulk microanalysis of assemblages of small fluid inclusions by LA-ICP-MS: Methodology and application to orogenic gold systems. Chem. Geol. 529, 119326. https://doi.org/10.1016/j.chemgeo.2019.119326.

Ujiie, K., 1997. Off-scraping accretionary process under the subduction of young oceanic crust: the Shimanto Belt of Okinawa, Ryukyu Arc. Tectonics 16, 305–322. https://doi.org/10.1029/96TC03367.

Ujiie, K., 2003. Deformation and fluid pressure variation during initiation and evolution of the plate boundary décollement zone in the Nankai accretionary prism. J. Geophys. Res. 108, 2398. https://doi.org/10.1029/2002JB002314.

Ujiie, K., Saishu, H., Fagereng, Å., Nishiyama, N., Otsubo, M., Masuyama, H., Kagi, H., 2018. An Explanation of Episodic Tremor and Slow Slip Constrained by Crack-Seal Veins and Viscous Shear in Subduction Mélange. Geophys. Res. Lett. 45, 5371–5379. https://doi.org/10.1029/2018GL078374.

Vrolijk, P., Myers, G., Moore, J.C., 1988. Warm fluid migration along tectonic melanges in the Kodiak Accretionary complex. J. Geophys. Res. 93, 10313–10324. https://doi.org/10.1029/JB093iB09p10313.

Vrolijk, P., Fisher, A., Gieskes, J., 1991. Geochemical and Geothermal Evidence for Fluid Migration in the Barbados Accretionary Prism, 18, pp. 947–950.

Wallace, L.M., Saffer, D.M., Barnes, P.M., Pecher, I.A., Petronotis, K.E., LeVay, L.J., Expedition 372/375 Scientists, 2019. Proceedings of the International Ocean Discovery Program Volume 372B/375. Proceedings of the International Ocean Discovery Program. International Ocean Discovery Program. https://doi.org/10.14379/iodp.proc.372B375.2019.

Westbrook, G.K., Smith, M.J., 1983. Long decollements and mud volcanoes: evidence from the Barbados Ridge complex for the role of high pore-fluid pressure in the development of an accretionary complex. Geol 11, 279. https://doi.org/10.1130/0091-7613(1983)11<279:LDAMVE>2.0.CO;2.

Wibberley, C.A.J., Shimamoto, T., 2003. Internal structure and permeability of major strike-slip fault zones: the median Tectonic Line in Mie Prefecture, Southwest Japan. J. Struct. Geol. 25, 59–78. https://doi.org/10.1016/S0191-8141(02)00014-7.

Williams, L.B., Hervig, R.L., Holloway, J.R., Hutcheon, I., 2001a. Boron isotope geochemistry during diagenesis. Part I. Experimental determination of fractionation during illitization of smectite. Geochim. Cosmochim. Acta 65, 1769–1782. https://doi.org/10.1016/S0016-7037(01)00557-9.

Williams, L.B., Hervig, R.L., Wieser, M.E., Hutcheon, I., 2001b. The influence of organic matter on the boron isotope geochemistry of the gulf coast sedimentary basin, USA. Chem. Geol. 174, 445–461. https://doi.org/10.1016/S0009-2541(00)00289-8.

Yoshida, K., Hirajima, T., Ohsawa, S., Kobayashi, T., Mishima, T., Sengen, Y., 2015. Geochemical features and relative B–Li–Cl compositions of deep-origin fluids trapped in high-pressure metamorphic rocks. Lithos 226, 50–64. https://doi.org/10.1016/j.lithos.2015.03.002.

You, C.-F., Gieskes, J.M., 2001. Hydrothermal alteration of hemi-pelagic sediments: experimental evaluation of geochemical processes in shallow subduction zones. Appl. Geochem. 16, 1055–1066. https://doi.org/10.1016/S0883-2927(01)00024-5.

You, C.-F., Spivack, A.J., Gieskes, J.M., Rosenbauer, R., 1995. Experimental study of boron geochemistry: Implications for fluid processes in subduction zones. Geochim. Cosmochim. Acta 59, 2435–2442.

Zack, T., John, T., 2007. An evaluation of reactive fluid flow and trace element mobility in subducting slabs. Chem. Geol. 239, 199–216. https://doi.org/10.1016/j.chemgeo.2006.10.020.

Zack, T., Tomascak, P.B., Rudnick, R.L., Dalpé, C., McDonough, W.F., 2003. Extremely light Li in orogenic eclogites: the role of isotope fractionation during dehydration in subducted oceanic crust. Earth Planet. Sci. Lett. 208, 279–290. https://doi.org/10.1016/S0012-821X(03)00035-9.